

3D characterization of polycrystalline
microstructure using a dual beam SEM-FIB
system

Master's Thesis



author:

Adrienn Baris

Materials Science MSc student

Supervisor: Károly Havancsák CSc

Eötvös University, Faculty of Science, Department of Materials Physics

Budapest, 2014

Contents

1	Introduction and goals	2
1.1	Introduction	2
1.2	Goals	3
2	Overview of the literature	5
2.1	Scanning electron microscopy	5
2.2	Physical background of scanning electron microscope	6
2.3	Electron backscatter diffraction	9
2.4	Focused ion beam tomography	10
3	Methods and equipments	13
3.1	FEI Quanta 3D FEG Scanning Electron Microscope	13
3.2	Electron Backscatter Diffraction	20
3.2.1	Physical background of EBSD	20
3.2.2	Image processing	31
3.2.3	Applications of EBSD	35
4	Results and discussion	40
4.1	Results	40
4.1.1	Sample preparation	40
4.1.2	Three dimensional reconstruction	47
4.2	Discussion	68
5	Acknowledgement	70

Chapter 1

Introduction and goals

1.1 Introduction

Most of the solid inorganic materials, such as metals, ceramics, semiconductors and minerals are polycrystalline, i.e., they are built up from many microscopic crystals (so-called grains or crystallites), which have different sizes and orientations. The description of orientation of grains has a very important role in materials science, physics, engineering and also in the industrial applications since many of the physical and chemical properties of polycrystalline materials (e.g., strength; chemical reactivity; magnetic susceptibility; deformability; resistance against stress, corrosion and cracking) depend on the distribution of crystalline orientation. The distribution of orientations is generally not random but has a preferred direction, in which case we say that the sample has texture. There are some methods to measure this texture and the grain structure of the sample, but these techniques give information about the *two-dimensional* (2D) structure or the resolution in the z-direction (depth-direction) is only of a few microns (as by the synchrotron X-ray diffraction).

In *scanning electron microscope* (SEM), the *electron backscattered diffraction* (EBSD) technique provides about 50 nm spatial resolution, but it informs us only about the upper 50 nm thick layer of the sample. Thus, if one is interested in the *three-dimensional* (3D) structure of the materials, he needs to develop a serial sectioning work using *focused ion beam (FIB) tomography*, meaning that the sample is sliced with defined and uniform steps and after every slice an EBSD measurement is performed. The next step is the processing of the recorded images and the visualization of the surface by a software dedicated to this task. The 3D microstructure

provides us complete information about the entire grain structure, the shape of the grains, and the character of the grain boundaries. It is also possible to measure the volume and area of the grains and the total number of neighbors.

1.2 Goals

The primary goal of my thesis is the reconstruction and 3D representation of a few μm^3 volume element in a given nickel sample using the focused ion beam tomography technique. Considering my limited time for the measurements and the reconstruction, the first task was the selection of the sample which complies with the following requirements:

- The grain size should not be too large so that the chosen volume could contain sufficient number of grains.
- The grain size should not be too small because the slice thickness decreases with the size of the smallest grain.
- The grains of the sample must have well-defined shape so that the process of reconstruction would not be highly difficult.

In this thesis, I will show that it is possible to reconstruct the desired volume by more than one mode and we can use various products from the specimen-electron beam or ion beam interaction in order to characterize the microstructure of the materials. These methods provide information about the grain structure by different mechanisms and depending on the information we are looking for, we can choose the appropriate one.

Another goal of my thesis is the presentation of sample preparation method that provides high quality surface, which is essential for high resolution EBSD measurements.

In the first part of my thesis, I give an overview of the history and basics of SEM, EBSD and FIB tomography techniques. During the measurements, I used a *FEI Quanta 3D SEM-FIB* dual beam system, which has numerous useful properties and applications that will be presented in the later sections. Afterwards, I will describe the physical background of EBSD and show the different methods of orientation determination. The second part of my thesis is devoted to the description of the

sample preparation and the selection of appropriate specimen. Furthermore, I describe the steps of the method that I used during the material characterization and I will show the results of the 3D microstructure reconstruction.

Chapter 2

Overview of the literature

2.1 Scanning electron microscopy

From the 1930s there was a strong need for a high resolution observation technique for solid samples. The discovery of electron and the fact that the wavelength of the electron is five orders of magnitude shorter than the wavelength of light opened a new opportunity in the development of materials investigation. The first transmission electron microscope was made by two German scientists, Ernst Ruska and Max Knoll in 1931. The first microscope model with different geometry was built in 1933 by Ruska [1]. This microscope provided the basic function of an average electron microscope but the maximal magnification was only 10x. At the same time Knoll started to work at Telefunken Company in the field of television design and in 1935 he constructed the first scanning electron microscope for the study of the television camera tubes. His development was based on deflection coils which moved the focused electron beam on the surface of the sample. In 1938 Manfred von Ardenne built scanning coils in the transmission electron microscope, thereby creating the first scanning transmission electron microscope (STEM). In 1942, Zworkyn and his co-workers built a dedicated scanning electron microscope. They found that secondary electrons cause the topographic contrast of the sample surface. The resolution of their scanning microscope was about 50 nm . The next significant step in the field of the development of secondary electron detector was in 1960, when Everhart and Thornley applied scintillator in order to improve the signal-noise ratio in a remarkable way. Around 1965 started the general use of the scanning electron microscope in the U.K., when the Cambridge Instrument Company created their

Stereoscan 1 SEM. Since then throughout the world, scientists use the scanning electron microscope not just for imaging but for element analysis using X-ray spectroscopy, nanofabricating with focused ion beam, texture analysis with backscatter electron diffraction, etc.

2.2 Physical background of scanning electron microscope

The schematic diagram of the electron column is depicted in Fig. 2.1. As it shown

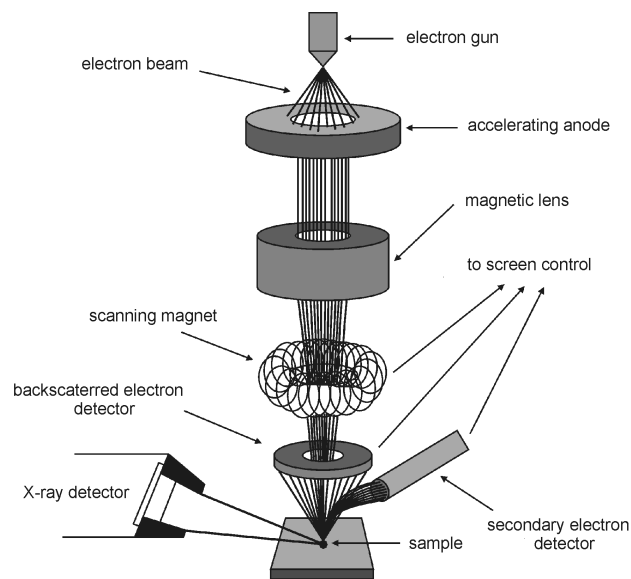


Figure 2.1: *The schematic illustration of the electron column.*

in the figure, the scanning microscope has scanning coils which moves the beam line by line on the sample surface. The image is then made by a generator which controls both the beam scanning and the pixels of the monitor at the same time. In every point, the detector collects the signals resulted by the sample-beam interactions. The detector signal modulates the intensity of each pixel, i.e., the change in the value of intensity indicates the change in the emission of the sample surface, which gives information about the number of the emitted electrons. The size of the image is kept at a fixed value because it is equal to the size of the monitor, therefore the magnification rate depends on the area of the scan (e.g., if we scan smaller area, the magnification increases). Obviously, for the proper and effective work, stable vacuum system is required around the source, at the lenses and coils, and in the sample chamber.

Figure 2.2 shows the primary electron beam-specimen interaction together with the generated products. The properties of these products will be described in later

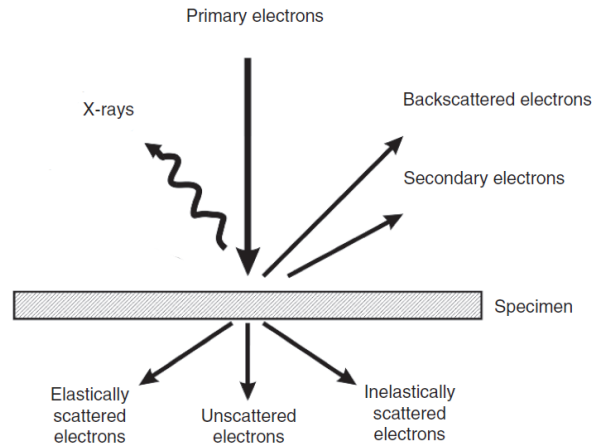


Figure 2.2: The schematic illustration of the generated particles by the primary beam in front of and behind the specimen.

sections. First, we review the two basic processes that are present when the beam penetrates in the sample:

1. *Elastic scattering on the atomic potential*

In this case the electrical field of the specimen atoms interacts with the entered electron in such way that the electron changes its path by wide-angle directional change and after numerous events the electron leaves the sample with negligible energy loss. Those elastically scattered electrons which leave the sample at an angle larger than 90° are called *backscattered electrons* (BSEs). The probability of elastic scattering is proportional to Z^2/E^2 , where Z denotes the atomic number and E is the electron energy. If the electron approaches heavy atom which has high atomic number and strong positive charge on the nucleus, the probability that the electron will be scattered elastically is greater than the inelastic scattering.

The cross-section of this interaction is given by

$$\sigma(> \phi_0) = 1.62 \cdot 10^{-20} \frac{Z^2}{E^2} \cot^2(\phi_0/2). \quad (2.1)$$

2. Inelastic electron-electron collision

An other interaction between the electron beam and the specimen is the inelastic electron-electron collision. During inelastic scattering, the primary electron penetrates into the sample through multiple atomic layers while it loses its energy gradually, and transferring this energy to the sample atoms [2]. Thus, electrons are ejected from the specimen atoms providing signals such as *secondary electrons* (SEs) and *X-rays*. The mathematical description of the electron energy loss (dE) during a unit of path length (ds) was given by Bethe:

$$\frac{dE}{ds} = -2\pi e^4 N_A \frac{Z\rho}{AE_e} \ln \left(\frac{1.166 E_e}{J} \right). \quad (2.2)$$

Equation 2.2 is the so-called *Bethe formula*, in which e is the charge of electron, N_A is Avogadro's constant, Z is the atomic number, ρ is the density of the specimen, A is the atomic weight, E_e is the primary electron beam energy and J is the average energy loss per collision. For most elements, the energy loss varies between 1 and 10 eV/nm , for an initial electron energy of 20 keV .

Further important quantities are the so-called *depth of penetration* and the *interaction volume*. Depth of penetration is determined by inelastic scattering and it describes that how deep the primary electrons can enter into the sample before losing their total energy. There is empirical formula given by Kanaya and Okayama for its value [3]:

$$R = \frac{0.0276 A E^{1.67}}{Z^{0.89} \rho} \quad (2.3)$$

where R is the penetration depth in the unit of μm . The interaction volume is in connection with the depth of penetration and gives the value of the size in which interactions can occur for various materials. The calculation of the volume size and shape is based on *Monte Carlo simulations*. The size of the interaction volume is of a few μm in general and it depends on the type of the specimen-electron interaction, the atomic number of the sample (the higher Z is, the smaller the interaction volume is), and the accelerating voltage. Both the entrance depth and the interaction volume depend on the angle of incidence. Equation 2.3 corresponds to a sample tilt of 0° .

2.3 Electron backscatter diffraction

The electron backscatter diffraction as it has been mentioned before in the introduction is a new and useful technique for the analysis of the grain orientation distribution, texture, phase identification and quantitative characterization of polycrystalline materials. Although the main application of EBSD is strongly associated today with SEM, the history of EBSD has interwoven with transmission electron microscopy (TEM) because the first observation of the so-called Kikuchi patterns was in 1928 when Shoji Nishikawa and Seishi Kikuchi captured it by backscattering mode in TEM [4]. They investigated a cleavage face of calcite with 50 keV electrons using cathode rays and the photographic recording film was placed in 6.4 cm behind and in front of the sample. Thus they captured the transmission patterns of the backscattered electrons from the specimen "which must have been produced by the electrons deflected through an angle greater than 90°". They observed these kind of patterns not only in calcite but also in mica sheet, topaz, quartz and zinc. They described the result as "black and white lines in pairs due to multiple scattering and selective reflection".

In 1937 Boersch studied cleaved, polished and etched samples (e.g., *NaCl*, *KCl*, *PbS*, *CaCO₃*, *CaF₂*, *quartz*, *mica*, *diamond*, *Cu*, *Fe*) at 20 kV, about 5° of incidence and up to an angle of 162°. The patterns he obtained were of high quality and rather sharp due to the applied vacuum in the chamber and that he removed the contamination from the specimen surface (Fig. 2.3) [5].

The first use of the term 'Electron Backscatter Kikuchi Pattern' (EBSP) and the first pattern indexing manual method was made by Venables who carried out his measurements with phosphor screen and TV camera [6]. The next significant step in the modernization of EBSD was in 1984 when Dingley used computer aided indexing and in 1986 the first commercial instrument by Link Analytical applied Dingley's software and hardware. In 1986 Niels Schmidt created a software for general indexing solution which means that it indexes all the known crystal systems and not the EBSP thus the process became faster and easier. The nowadays EBSD technique is based on the so-called *orientation map* (OM) or *orientation imaging microscopy* (OIM) where the electron beam scans the sample point by point and the computer indexes the Kikuchi patterns (which appear on the phosphor screen) in each point on the chosen scanned area of the sample. OM is a colored orientation

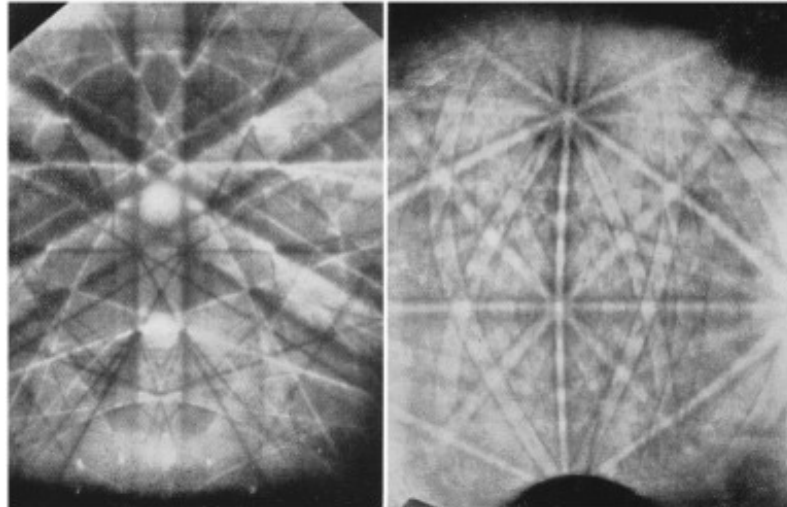


Figure 2.3: *First high quality Kikuchi patterns by Boersch from iron (left) and fluorite (right) [5].*

representation of a given point of the surface. The detailed description of the physical basis of EBSD can be found in Chapter 3.2.

2.4 Focused ion beam tomography

Focused ion beam tomography or FIB tomography is the generic name of those methods which provide microstructural, crystallographic and/or chemical informations about the materials in all the three dimensions using high energy focused ion beam. This technique is based on high energy, precisely focused beam of ions (generally Ga^+). In the modern SEM systems the generally used ion source is a *liquid metal ion source* (LMIS) and depending on the accelerating voltage and the ion current the FIB can be used for imaging or milling.

This is a young technique and its application in scanning electron microscope traced back to 1998. The first application of FIB tomography was in 1982 when Patkin and Morrison [7] combined single beam FIB with secondary ion mass spectroscopy (SIMS). Ten years later Hutter and Grasserbauer developed the FIB-SIMS system and the lateral resolution reached the few μm but the depth resolution was undefined due to the sputtered deposition. When the FIB systems became better in the resolution and more accurate in the 1990s, the next development in the area of the FIB-SIMS technique was the so-called 'shave-off' depth-profiling method which is a sequential mapping procedure. It contains two steps: in the first the ion beam

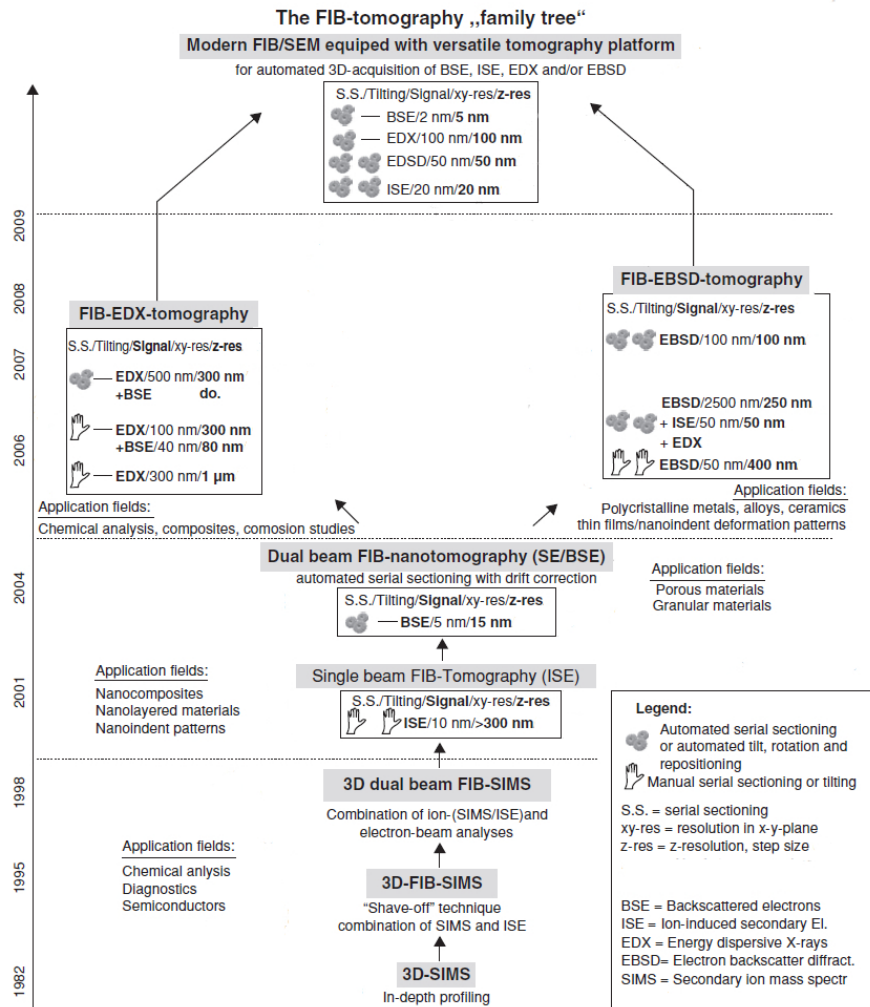


Figure 2.4: The chronological development of the FIB tomography and its applications.

strikes the sample perpendicular to the surface and in the second step the sample is tilted by 90 degrees (parallel to the beam) and thus the beam sweeps away the sputtered components and the upper layer of the sample surface [8]. The measurements and the mapping required sample moving, tilting and repositioning, thus it was very slow and time consuming. In 1998 the first dual beam FIB-SEM-SIMS system appeared due to the work of Sakamoto et al. [9]. The system allowed to obtain 3D chemical and structural data using the SIMS measurements and the secondary electron images from the same area. This procedure is also time consuming due to the shave-off method followed by a new imaging step in an other position. The application fields of the method are the 3D chemical analysis and diagnostics of integrated circuit or other semiconductor products.

Figure 2.4 shows the chronological evolution of the FIB tomography and – as shown in figure – depending on the used signal from the observed materials (like ion-induced secondary electrons, energy dispersive X-ray spectrum, electron backscatter diffraction) the FIB tomography can be applied in various fields. In the beginning of the 2000s the FIB tomography became basically a manual serial sectioning method where the serial 'cut - tilt and positioning - imaging/measure - tilt and positioning - cut' process was repeated manually which caused slow, less accurate and lower z-resolution (few 100 nm) reconstructions. It resulted in a fundamental need for the faster and more precise automatized procedure in the field of the investigation of nanostructures where the average object size is smaller than the cutting steps. The solution was to write scripts to the machine that contain the execution actions but the main problem was the precise automated positioning. Two processes were born: positioning by drift correction using pattern recognition [11] and the shape observe technique which uses markers [12]. The reached z-resolution in the case of backscatter electron images is 5 nm [10].

A new and very useful application of the FIB tomography is the 3D grain- and microstructure reconstruction of polycrystalline materials using EBSD measurements. We have the opportunity to combine it with EDS mapping, BSE and ISE imaging in order to gain more complete information. It has also two modes for the serial section process, in the manually mode the reached z-resolution is about 400 nm and in the automated mode it is about 50 nm [10]. During my work I applied manual adjusted EBSD based FIB tomography. Although the manual tomography is slower and the available resolution is lower, we believe that it can give a deeper understanding and insight of how the process works and it is an appropriate way for gain experience in the usage of FIB tomography technique. In the following, I give a detailed description of the applied process.

Chapter 3

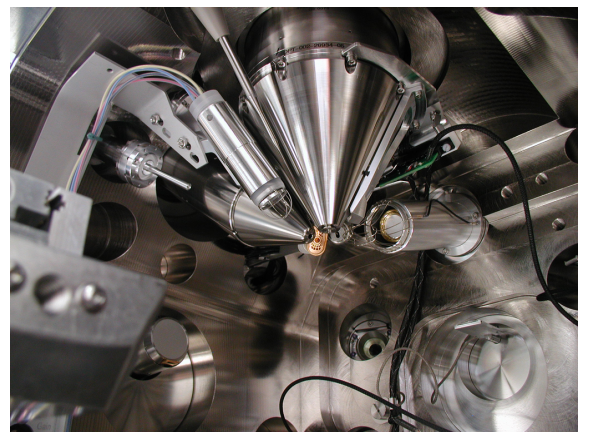
Methods and equipments

3.1 FEI Quanta 3D FEG Scanning Electron Microscope

The FEI Quanta SEM-FIB system (Fig. 3.1) is a *state of the art*, high resolution dual beam scanning electron microscope. The dual beam phrase means that, in addition to the electron gun, the microscope also has an ion source. These two guns are suitable for imaging, and by using FIB, we can sputter the sample as well as mill and cut into it. The source of the electrons is a *Schottky-source*, that is a



(a)



(b)

Figure 3.1: *The 3D Quanta 3D FEG dual beam scanning electron microscope (a) and inside of it (b).*

type of thermal field emission cathode or a field emission gun (FEG). It is made of tungsten single crystal ((110) plain), coated with thin layer zirconium dioxide in order to decrease the electron work function. In the electron gun electrons leave the cathode, due to the heating (1800 K) and the applied high electric field ($\sim 5 \text{ kV}$). The accelerating voltage is between 2 kV and 30 kV . The diameter of the first beam crossing (the name of which is *crossover*) in the gun is $10 - 20 \text{ nm}$, which are projected by electric lenses to the sample surface. In this way, the diameter of the spot on the surface is about 1 nm , which is the nominal (ultimate maximal) resolution of this microscope. These magnetic lenses are based on the Lorentz force ($\vec{F} = e(\vec{v} \times \vec{B})$), resulting in an spiral trajectory inside the lenses of the accelerated electrons. Both the focal length of the lenses can be adjusted by the magnitude of the current in the electromagnets.

There are products of different types emitted from the sample surface due the electron beam-sample interaction (Fig. 2.2): such as the *secondary electrons*, *backscattered electrons* and *X-ray photons*. These products have different properties, therefore different detectors are required in order to observe them. Since these products are generated in a thin layer of the sample surface, we can detect them from the side of the incoming beam. In Fig. 2.2, we also indicated those particles, that are generated by the primary beam and emitted on the opposite side of the sample. In the scanning electron microscope, we usually study bulk specimens, and therefore these types of particles cannot be detected as the beam is not able to pass through the sample. A scanning transmission electron detector is also implemented in the FEI Quanta 3D instrument for investigating thin samples ($< 100 \text{ nm}$). Let us see the detailed description of the products.

- *Secondary electrons*

Secondary electrons are produced by inelastic interaction between the primary beam and the sample atoms. These electrons are located in the outer shells of the atoms and thus being weakly bounded to it. They have a kinetic energy of $5 - 10 \text{ eV}$, which is the lowest compared to other product particles. Therefore, they give information about the upper few nm thickness layer of the surface, and provide topographical information. The maximum spatial resolution in this case is about 1 nm . The most frequently used secondary electron detector is the previously mentioned *Everhart-Thornley detector* (ETD) (Fig. 3.2).

This detector is built up from a relatively low positively biased Faraday cage (that attracts low energy secondary electrons) and a highly biased scintillator converting the entering electrons to photons. These photons are guided by an optical waveguide towards a photomultiplier tube, where the signal is amplified by several dynodes based on the photoelectric effect.

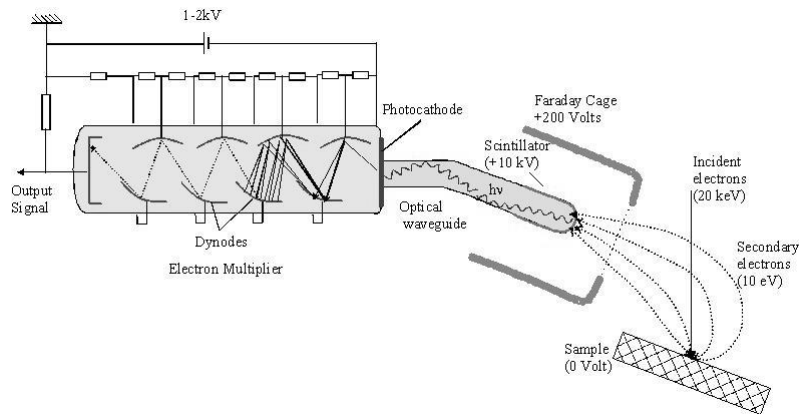


Figure 3.2: *Illustration of the Everhart–Thornley detector [13].*

- *Backscattered electrons*

As it was mentioned before, the backscattered electrons come from the deeper parts of the sample, originated from the primary beam and they leave the sample at an angle greater than 90° . They are exposed only to elastic scattering, therefore they leave the sample with negligible energy loss. These electrons reach the detector with an energy of the order of magnitude of 10 keV . BSE signals are useful, due to the fact that the yield of these electrons depends on the atomic number. Thus, we are able to distinguish material regions that are built up from different chemical elements. The contrast difference due to the atomic number does not depend on the beam energy. Besides of image recording, we can use the BSE signal for diffraction measurements. In case of BSE images the resolution is about $2 - 4\text{ nm}$, depending on the properties of the sample and the energy of the incident beam. ETD can be used for detection of BSEs alone too if a low negative bias is applied, since the BSEs have energy enough to reach the detector, since in this case, SEs are repelled from the detector. In general, we use two kinds of detectors in the FEI Quanta 3D SEM for observing BSEs: *backscattered electron detector* (BSED) and *low voltage high contrast detector* or vCD (Fig. 3.3).

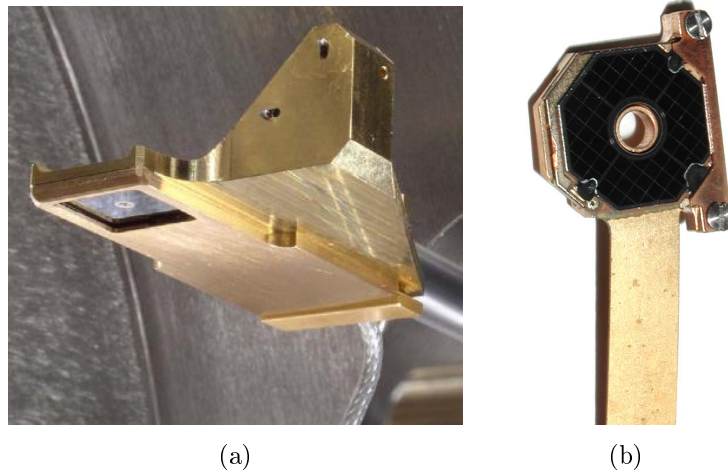


Figure 3.3: *The two BSE detectors: vCD (a), BSED (b).*

vCD is a retractable detector used for the efficient detection of low energy BSEs (with a threshold energy of 3 keV), and provides both element contrast and topological details. BSED is a four-segment semiconductor detector, that is located above the specimen, concentrically around the incident beam. It is capable to detect those BSEs having energy larger than 5 keV . These electrons generate electron-hole pairs in the semiconductor material of the detector, which are then separated and collected when voltage is applied on the diode and the resulting impulse is used for image recording.

- *X-ray photons*

The incident beam has energy enough for the extrusion of electrons from an inner shell of the atom. In this case, the atom loses its stability, and the rearrangement of electron structure occurs during which an electron from a higher energy level fills the place of the rejected electron. As a result of this process, the energy difference between the two energy levels appears in the form of X-ray photon. The energy of the photon is characteristic of the emitting atom. By measuring of the energy and amount of the X-ray photons we can gain information about the elemental composition, thus X-ray photons provide both quantitative and qualitative data. The FEI Quanta 3D SEM is equipped with *energy dispersive X-ray detector* (EDX) for chemical analysis, which is a high-purity silicon drift detector.

As it has been mentioned above, applied vacuum is crucial for stable working

of an electron microscope. The value of the pressure varies at different locations of the column. The highest vacuum value is at the source area, which is $10^{-7} Pa$. Furthermore, the vacuum is less at the magnetic lenses ($10^{-5} Pa$) and the smallest vacuum is in the sample chamber ($10^{-3} Pa$). The last value corresponds only to high vacuum operating mode. The FEI Quanta 3D SEM has three different operating mode, such as: high vacuum mode, low vacuum and environmental mode. In low vacuum operating mode, the pressure in the chamber is $10 - 130 Pa$ and we can observe uncoated, non-conductive samples due to the neutralizing effect of the water vapor. The environmental vacuum mode (pressure is between $130 - 2600 Pa$) provides opportunity to analyze biological samples or other specimens containing moisture and wet (since the humidity in the chamber is close to 100%), and also a controllable temperature by the use of a Peltier stage.

The setup of focused ion column is very similar to that of the electron, as it is shown in Fig. 3.4. Ions have various usage possibility such as imaging, milling, nanofabrication, nanolithography using chemical vapor deposition, making cross-section samples or TEM lamella and 3D tomography (the reconstruction via ion generated images will be describe in Section 4.1.2). The process of the imaging happens by the same way as in the case of the usage of electrons. For imaging we can use *Continuous Dynode Electron Multiplier* (CDEM) which takes place near to the ion column. CDEM differs from the ETD used multiplier having a continuous dynode system and it capable measuring both SEs and SIs.

As described in the introduction, ions are generated by a liquid ion source. In the Quanta 3D FIB system, a tungsten needle is attached to a reservoir which holds the gallium source. Gallium has many useful properties that explain its widespread usage. Just to mention some of these: since its low melting point ($29.8^{\circ}C$), the heating is fast and the Ga does not react with the tungsten; it has low volatility at the melting point that provides long source life and conserves the supply of metal; its low vapor pressure gives long lifetime, because the liquid will not evaporate; it has exceptional super-cooling properties, as it stays in the liquid phase for weeks after being melted; its electrical, mechanical and vacuum properties are outstanding. Schematic illustration of the structure of the ion gun and a photo of the tungsten needle are shown in Fig. 3.5.

The Ga^{+} emission process consists of two main steps that can be described as

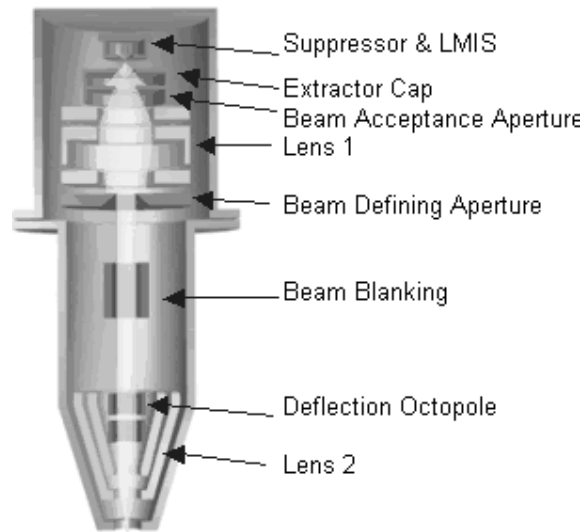


Figure 3.4: Schematic figure of an ion column [14].

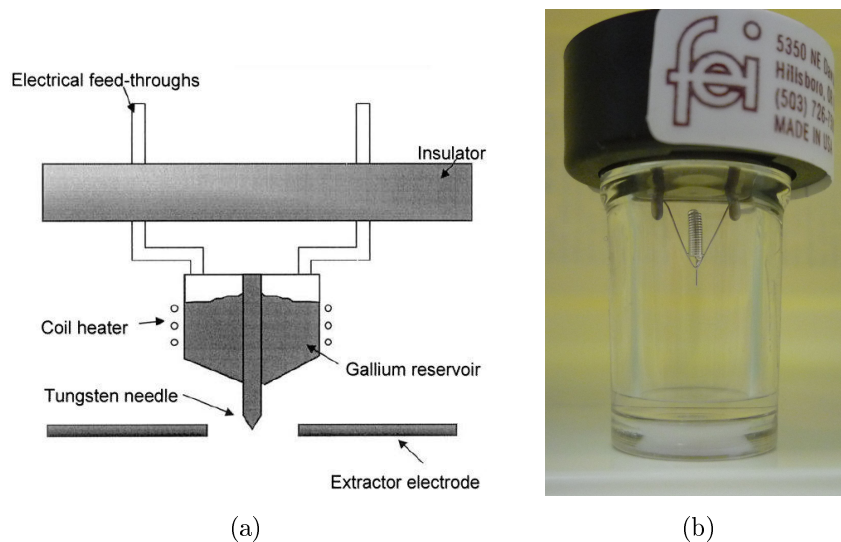


Figure 3.5: Schematic illustration of Ga ion source (a) [14] and the Ga container spiral with the tungsten tip itself of our microscope (b).

follows. First, gallium is heated by coil heaters, as a result gallium starts to flow and wets the tungsten needle. The needle tip radius is about $2 - 5 \mu\text{m}$ and the applied electric field is in the order of 10^8 V/cm causing a point source in the end of the wetted tip. The point size is between $2 - 5 \text{ nm}$ with a conical shape. In the next step, an applied extraction voltage pulls out gallium from the end of the tungsten tip. The acceleration voltage can be modified between $2 - 30 \text{ kV}$ and the value of the ion current is adjustable by apertures between 1.5 pA and 65 nA . There are

two lenses: the *condensor lens* forms and the *objective lens* focuses the beam. The interaction between the ion beam and the sample also generates various particles, e.g., secondary electrons, secondary ions (SI), sputtered atoms and molecules from the sample material. Besides of the sputtering, the higher energy ions are able to implant to the deeper regions of the specimen, during which they lose their total energy. The depth of penetration depends on the initial energy of the ion as well as on the angle between the incidence beam and the surface of the sample, and it is typically in the order of a few 100 nm . Figure 3.6 shows the products of elastic ion-atom collision and illustrates the sputtering by higher energy ion beam.

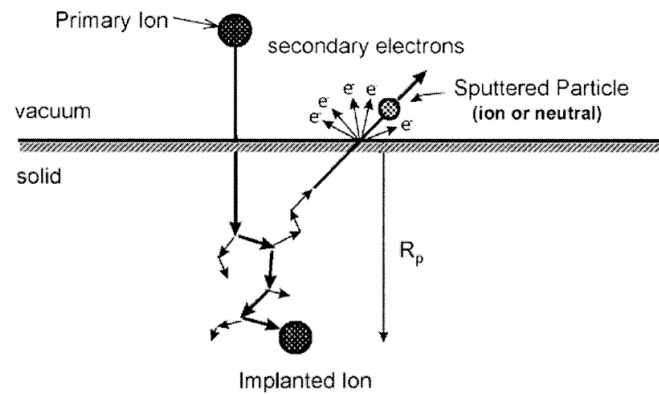


Figure 3.6: *Illustration of the products generated by the interaction of ion beam and the sample [14].*

There are some artifacts during sample preparation using the FIB system, such as the redeposition of the removed material and the appearance of amorphous phase. In order to prevent the removed material from overlaying the area of interest on the sample, we have to prepare an area larger than the originally requested; or to reduce the milling rate.

The greatest advantage of dual beam systems that while FIB prepares the sample, the electron beam can be used for imaging and monitoring the process without moving the stage. In the FEI Quanta 3D SEM-FIB system, the focus point of two focal beams are in coincidence if the sample is at the eucentric height. The structure of the system is such that if the sample is tilted at 52° relative to the electron beam, then its position is normal to the ion beam (Fig. 3.7).

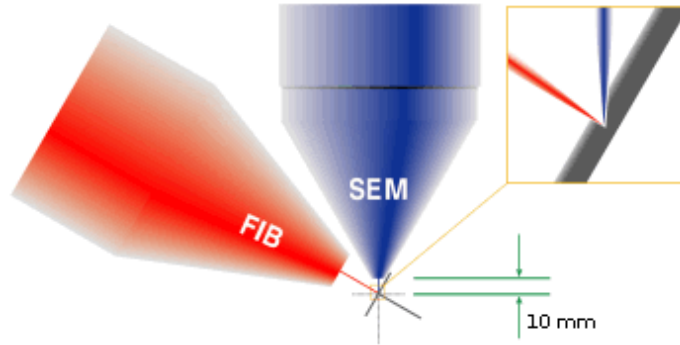


Figure 3.7: *Schematic representation of a dual beam setup.*

3.2 Electron Backscatter Diffraction

3.2.1 Physical background of EBSD

According to Section 3.1, the energy of incoming electron beam in the SEM is between 2 and 30 keV , which is enough to approach the inner part of the atoms where the positive charge is only partially shielded by the electrons of the atom. Therefore, the beam electrons perceive strong Coulomb field, on which these electrons are elastically scattered and they can leave the sample through the surface. These are the backscattered electrons that we use for the EBSD measurements. During the EBSD measurement, the sample surface is not held horizontally, but tilted relative to the incoming beam, since with increasing tilting angle the intensity of the backscattered electron beam increases. This effect is shown in Fig. 3.8. The maximum intensity can be achieved near 70° , thus the surface of the sample is generally at this angle during the measurement, which is illustrated in Fig. 3.9.

With this setup, the incoming electron beam is not able to penetrate deeply into the specimen, but it scatters back from a shallow layer beneath the surface of the sample. The thickness of this layer depends on the material, but it is typically between 10 – 50 nm . Figure 3.10 shows the electron energy distribution at 0° and 70° sample tilting in case of 20 keV incoming beam energy. If the sample is tilted at 70° , the majority of the backscattered beam contains electrons of energy near 20 keV and a negligible energy loss during the penetration.

Diffraction pattern, which is created by the interference of backscattered electrons are detected with a special detector, the so-called *Hikari camera*. The surface of the detector is covered with fluorescent substance. The fluorescent screen – on

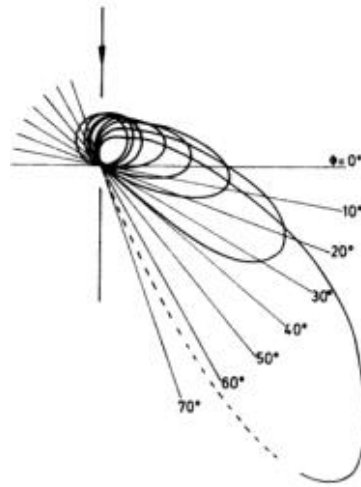


Figure 3.8: *The yield of the backscattered electrons increase with the sample tilting angle [15].*

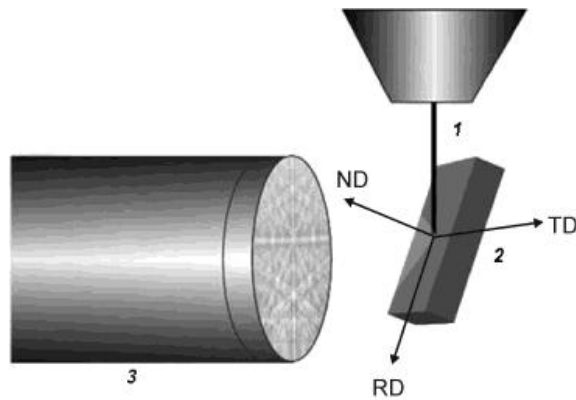


Figure 3.9: *Illustration of the sample position during an EBSD measurement. Incoming electron beam (1), sample (2) and the Hikari camera (3).*

which the diffraction pattern evolves – is transparent, thus a CCD camera can capture a series of recordings from behind the screen. Images captured by the CCD camera are processed by a computer in digital form. For the EBSD measurements, I used a Hikari camera with OIM 5.2 software produced by the EDAX Company. A photo of the Hikari camera and the schematic figure of the EDAX-FEI system are shown in Fig. 3.11.

Short description of TEM diffraction

In order to understand the emerging diffraction patterns in the SEM, let us begin with the single crystal diffraction measured by TEM. The point-like diffraction max-

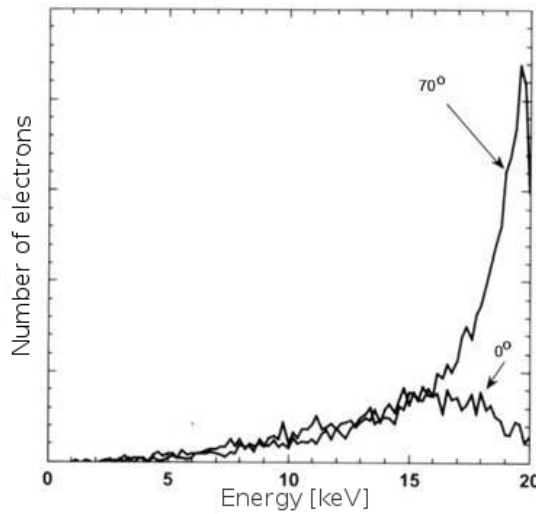


Figure 3.10: *Electron energy distribution at 0° and 70° sample tilting.*

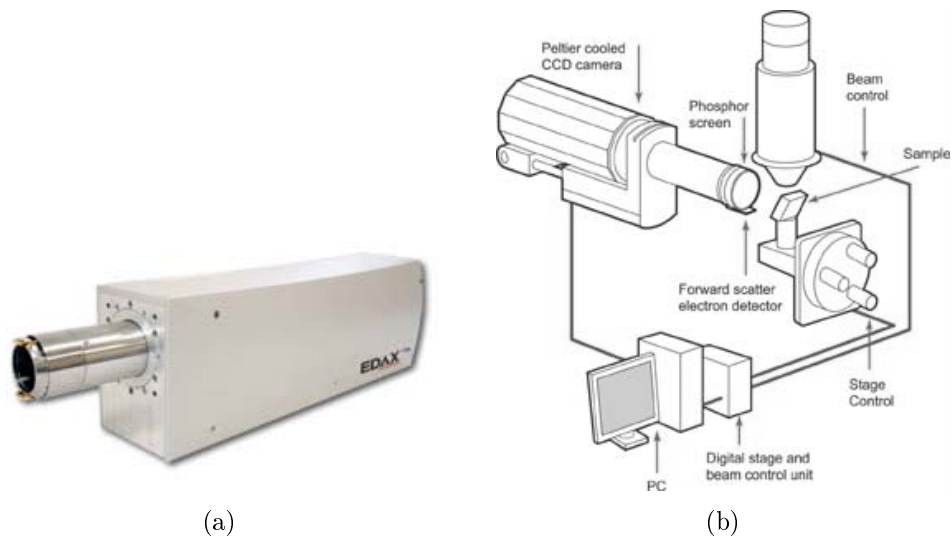


Figure 3.11: *EDAX Hikari camera (a) and an illustration of the FEI-EDAX setup (b).*

ima in TEM are shown in Fig. 3.12, for the case of a usual thin sample ($< 100 \text{ nm}$). The diffraction maxima are created by the following process: the electrons of the incoming beam are elastically scattered on the Coulomb field of the specimen atoms, then these leave the sample while the electron waves interfere with each other. Compared to the lattice constant, the detector screen is located at a large distance from the sample, thus the interfering beams are approximately parallel (and they are therefore presented by the interference of parallel beams in the mathematical description of the phenomena). The name of this phenomenon is – adapted from

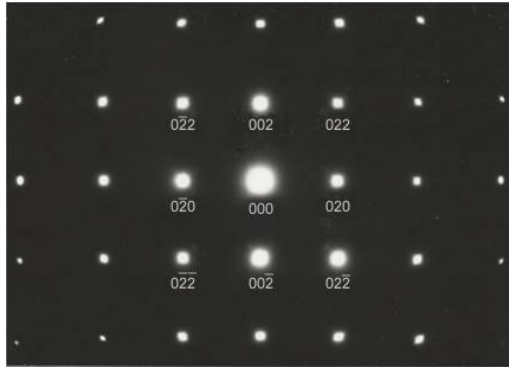


Figure 3.12: *Diffraction pattern in a transmission electron microscope of an FCC single crystal with the incoming beam pointing to the (100) crystallographic direction.*

optics – Fraunhofer diffraction. The result of the interference in most directions is destructive, thus in these directions the detector measures only low background values. However, in some directions, the interference is constructive. These directions are labelled as Bragg’s directions and the phenomenon is called Bragg scattering, named after Bragg who was the first to describe this process. Using the mathematical methods of the elastic electron scattering and the interference, the Bragg’s directions can be calculated in case of a given crystal. The scattering on the atoms results in maximum intensity in that directions, as if the incoming beam would be reflected from planes which are occupied by atoms. This is shown in Fig. 3.13, where \vec{k}_0 indicates the direction of the incoming beam and \vec{k} indicates the beam that is scattered in the Bragg direction. Obviously, the real physical process is not

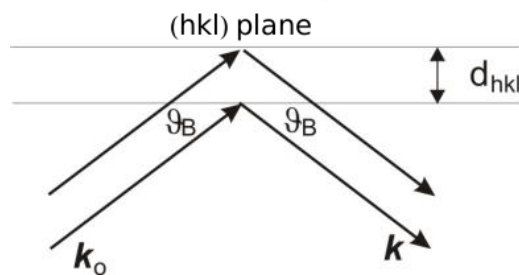


Figure 3.13: *The incoming (\vec{k}_0) and the scattered (\vec{k}) beam in case of constructive interference.*

reflection, but we can use this approximation for the efficient calculation of the directions of the constructive interference. In addition to the symmetrical position of the beam, it is also necessary for the constructive interference that the difference between the path of the incoming beams from the neighboring planes be an integer

multiple of the wavelength. The angles of the direction of constructive interference are given by Bragg:

$$2d_{hkl} \sin \vartheta_B = n\lambda, \quad (3.1)$$

where λ is the wavelength of the electron beam, d_{hkl} is the spacing between the planes in the atomic lattice, ϑ_B is the angle between the scattering planes and the incident beam and n is the order of the reflection. Equation 3.1 is known as the Bragg's law named after William Henry Bragg and his son William Lawrence Bragg, who were awarded the Nobel Prize in 1915 for their contributions to crystal structure analysis. Bragg diffraction can be used by any other electromagnetic radiation or subatomic particle waves with wavelength comparable to atomic spacing. As a result of the Bragg reflection, we get a diffraction point from the parallel atomic planes, as it is shown in Fig. 3.13. We describe these planes by three numbers: by the so-called *Miller indices* (hkl). The point (000) is the starting point of the diffraction pattern and it corresponds to the direct beam that passed through without deflection. For practical purposes, it is also worth defining another lattice that represents the crystallographic planes. In the diffraction figure we can see a plane, or more precisely some points of the plane of this lattice. The name of the lattice is *reciprocal lattice* and there is a well-defined relationship between that and the geometric structure of the original crystal lattice. The original lattice or *direct lattice* can be described by the $\vec{a}_1, \vec{a}_2, \vec{a}_3$ basis vectors. We can define the basis vectors of the reciprocal lattice by the following:

$$\vec{b}_i = \frac{\vec{a}_j \times \vec{a}_k}{\vec{a}_i(\vec{a}_j \times \vec{a}_k)}. \quad (3.2)$$

Different crystal lattices have different reciprocal lattices and if the direct crystal is rotated, the reciprocal lattice also turns with it. Thus, the lattice structure (and even the orientation of the crystal) is characterized by the arrangement of the diffraction points. Since the wavelength of the electron is small compared to the lattice constant and the parallel incoming beam, together with the fact that the Bragg angle is small ($< 1^\circ$), those scattering planes from which the diffraction spots originate are approximately perpendicular to the detector surface.

Kikuchi lines in the TEM

If we observe a thicker sample ($> 100\text{ nm}$) in the TEM, dark and bright line pairs appear in addition to the diffraction spots, which lines are the so-called Kikuchi lines. As the thickness of the sample increases, the phenomenon becomes more pronounced. If the sample thickness reaches (or exceeds) 200 nm , the diffraction points disappear and only the Kikuchi lines remain noticeable. Figure 3.14 shows this scenario.

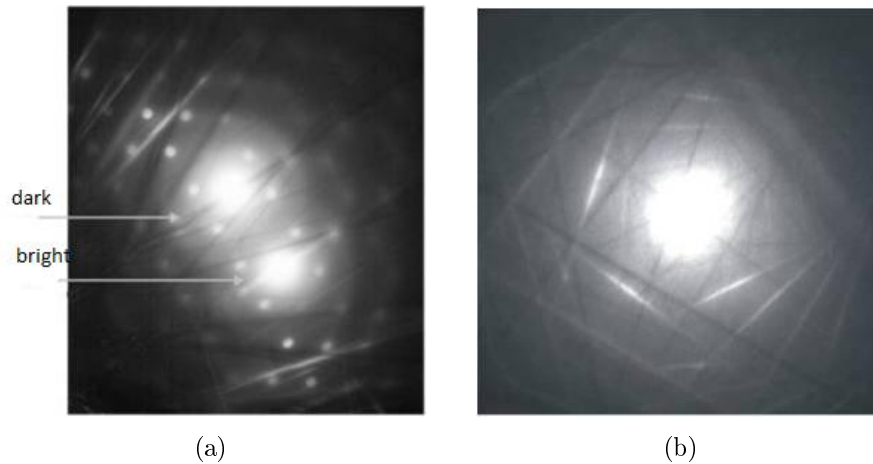


Figure 3.14: *Kikuchi lines in the case of a thicker sample.*

The formation of the line pairs is rather clear if we consider that the probability of inelastic and multiple scattering of electrons increases in case of a thicker sample. For electrons, this probability is much higher than that of the scattering of X-ray waves. The reason is that the Coulomb field of the crystal on which the electrons scatter is present everywhere, but the X-ray photons can be scattered only by electrons. The result of many consecutive elastic scattering is that inside the thick crystal, electrons are moving in all directions, thus onto a given scattering plane, they come from multiple directions. Obviously, electrons with the highest intensity arrive from the direction of the original incoming beam. In addition to the multiple elastic scattering, there is also inelastic scattering, however, during this process the electron energy loss is small ($10 - 20\text{ eV}$) compared to the incoming beam energy ($100 - 400\text{ keV}$). Therefore the wavelength of these electrons is practically unchanged and these electrons remain to be able to interfere.

The electrons scattered on the planes under the Bragg angle are coming not only from a single direction but from all along the cone surfaces at both sides of the

diffracting plane with a half-cone angle of $90^\circ - \vartheta_B$ (see Fig. 3.15). These cones are the so-called *Kossel cones*. Due to the beams that pass along the cones' surface and

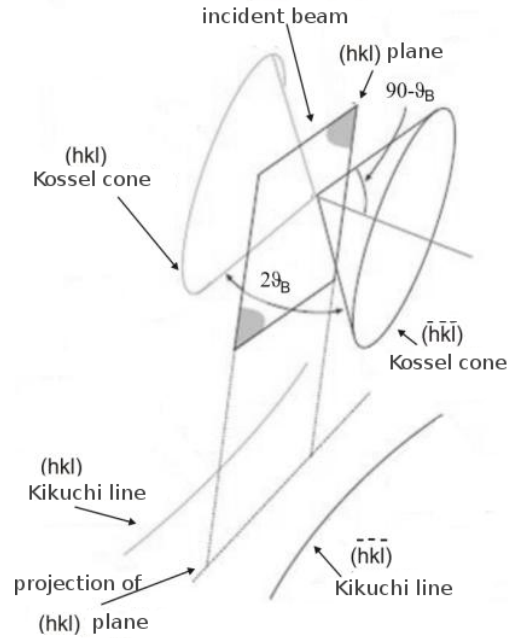


Figure 3.15: *The Kossel cones.*

arrive at the Bragg angle, the scattered beam complies with the condition of the constructive interference, which has a hyperbole trace on the surface of the detector. As the Bragg angle is small and the detector screen is small compared to the size of the cone, this hyperbolic arc resembles a line on the diffraction image. Those beams that move along the close cones to the original incoming beam direction have stronger intensity than that of the beams from cones with other direction. Therefore, a bright straight line emerges from the background on the screen of the detector, as a sign of its trace (*hkl* Kikuchi line). This intensity will be absent on the other side of the plane, where it would otherwise appear without the Bragg reflection. Due to the fact that the other cone intensity cannot compensate this absence of intensity, the another cone trace will be a dark straight line compared to the background (\overline{hkl} Kikuchi line). The bright line is always located further away from the bright spot of the direct beam, while the the dark line is located close to the spot. Based on the above, the projection of the diffractive plane (which of course is not shown in the diffraction pattern) intersects with the detector surface at the half of the distance between the bright and dark line pairs. If the plane is rotated, the pairs of the lines

follow the rotation, because their position is always exactly determined by the Bragg angle. The position of the line pairs is strictly determined by the position of the crystal. The simple theory that was outlined here is known as the *kinematic theory*.

Kikuchi patterns in SEM

It is worth devoting some lines to the physical explanation of the process that leads to the occurrence of Kikuchi patterns in SEM. According to the previous section, it can be easily understood since the physical background is the same as in the TEM, but the geometry is different. In the case of the SEM EBSD measurements, the bright spot of direct beam does not appear on the detector screen, due to the geometrical arrangement and the use of the backscattered electrons (Fig. 3.16).

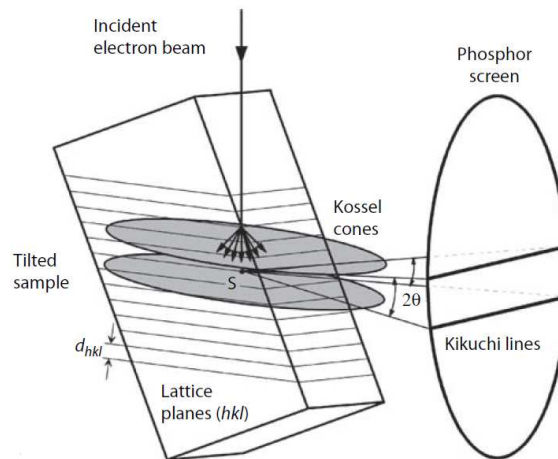


Figure 3.16: *The path of the beams during the EBSD measurement.*

The question is what kind of diffraction pattern can occur in SEM? As we have seen in the case of the TEM, due to the multiple scattering, electrons that move in all directions within the crystal and the ones that move in the Bragg direction, will move along the surface of the two Kossel cones. Thus, the lines of intersection of the two cones and the surface of the detector appear on the screen of the detector. Since the diffraction angle is small, the intersection here also resembles a straight line. In this case we are away from the direction of direct beam, therefore there is no significant intensity difference between the two lines. The two cones are located on the two sides of the diffraction plane, and the intersection of the detector surface and the plane – which is not visible – is in the half of the distance between the two

lines. The two parallel lines create a band, that is called the Kikuchi band. The width of bands can be easily estimated by the kinematic theory. As the Bragg angle is small, $\sin \vartheta_B$ in Eq. (3.1) can be approximated by ϑ_B and we get

$$2\vartheta_B \cong \frac{\lambda}{d_{hkl}}. \quad (3.3)$$

In this approximation, the width of the bands is proportional to the Bragg angle (the actual distance depends on the detector-sample distance). This means that there is an inverse relation between the spacing of the planes and the width of bands, i.e., the bigger the spacing between the neighboring planes is, the narrower the width of the Kikuchi band is. We obtain Kikuchi bands from all of the crystal planes whose theoretical extension can intersect the detector screen. Figure 3.17 shows the expected pattern on the basis of the above simple kinematic model as well as a diffraction pattern from a measurement.

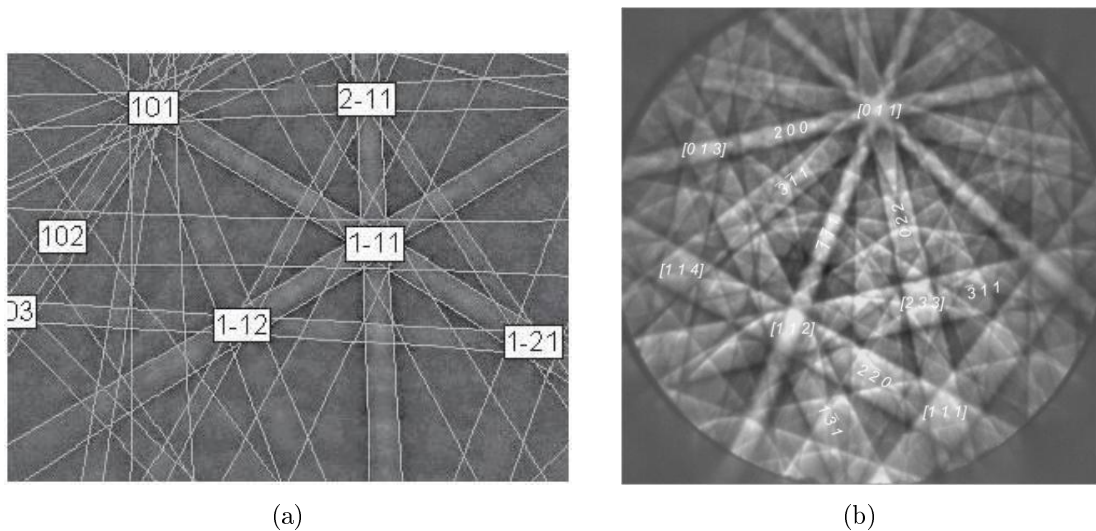


Figure 3.17: *The expected Kikuchi pattern on the basis of the kinematic model (from simulations) (a) and the real EBSD pattern (b) of an FCC crystal.*

As it is shown, the real pattern is more complex than what is expected from kinematic model. However, the bands are clearly visible and the result of the simple kinematic simulation also shows that there are wider and narrower Kikuchi bands.

We can compare an EBSD image with an image produced by the computer simulation and then we can inscribe the Miller indices of the crystal planes on the bands (Fig. 3.17b). The meeting points of the bands assign crystallographic directions which are the so-called *zone axes*. Figure 3.17 shows that the zone axis $[011]$ is the

intersection of (among others) the planes (200), (311), (022). In modern EBSD systems, the computer identifies the Kikuchi bands and the zone axes. Theoretically, for the determination of the appropriate orientation of the investigated small single crystal volume, the identification of at least three bands or zone axes are necessary. However, the situation is much less ideal in real measurements. In practice, due to measurement errors, it is generally necessary to identify more than three bands and zone axes (details of the EBSD data processing will be described later).

The complexity of experimentally measured Kikuchi patterns shows that the outlined simple theory is appropriate only partially for the explanation of the characteristics of backscattered electron diffraction image. In the kinematic model, only the geometric properties of Bragg diffraction are taken into account, therefore it is not suitable for the correct description of the intensity relations. The model provides satisfying predictions regarding the position and width of the bands, however, it does not accounts correctly for the intensity of the backscattered electrons within the bands. Figure 3.17b shows clearly that there are dark lines on the two sides of the bands, although we would expect here maximum intensity by the kinematic theory. Towards the correct description of the intensity relations, we have to use the so-called *dynamic model* of scattering, that takes multiple and inelastic scattering into account. Furthermore, it also considers that when the electron is entering the sample, it experiences a periodic crystal potential. For the description of the real structure of the Kikuchi patterns, we have to solve the Schrödinger equation with the proper boundary conditions at the crystal-vacuum interface. The Schrödinger equation for the electron which enters the crystal is

$$\left(-\frac{\hbar^2}{2m}\nabla^2 + V(r)\right)\Psi(r) = E\Psi(r), \quad (3.4)$$

in which $\Psi(r)$ is the wave function of one electron and $V(r)$ is the periodic lattice potential (i.e., $V(r) = V(r + R)$, where R is the lattice vector). Due to the potential energy is periodic, the plane wave expansion contains only plain waves that will be determined by the lattice periodicity. We can use the Fourier expansion for the potential that gives the following:

$$\nabla^2\Psi + \frac{2m}{\hbar^2}\left(E - \sum_g V_g e^{2\pi gr}\right)\Psi = 0, \quad (3.5)$$

where g is the reciprocal lattice vector. The mathematical treatment of the dynamic

model is complex and an analytic solution is not possible. However, using computer based, approximate solutions, one can simulate the experimental diffraction images. Due to the complex nature of the model, I will mention here only the most important features. The description of electrons moving in periodic potential is known from solid state physics. The Nobel Prize laureate *Felix Bloch* was the one who proved that the solutions of the Schrödinger equation are special plane waves, whose amplitude changes according to a lattice periodic function. These functions are called the *Bloch functions* and their linear combination provides the general solution of the electron waves. This is also valid for the electrons entering the sample, as the periodic potential allows for the movement of waves only of the form of the Bloch functions.

What happens when the monochromatic electron beam enters the sample? The beam splits into plane waves, whose amplitude varies according to lattice periodic function. Due to the periodic lattice potential, the kinetic energy of the waves change only a few eV , which is very small compared to the incident beam energy ($20 - 30 keV$). The magnitude of the lattice potential is in the order of eV . The question is how many waves are formed when the incoming beam splits. According to the Bloch solution, as many as the number of the plane series is in the lattice. In other words, we can say that as many as the number of the reciprocal lattice points are in the reciprocal lattice according to the crystal. Let us assume that the number of these points is n . Thus, n number of waves travel in all Bragg directions with slightly different wavelengths, and the interference of these produces the resulting intensity in a given direction. In the simulations, it is not necessary to consider all of these waves, as there are both intense and less intense waves and for results satisfying enough, only about 100 wave components are needed. Since analytical treatment is not feasible, we rely on computer simulations. Figure 3.18 shows the comparison of the simulations (based on the dynamic model) and the Kikuchi pattern of an actual EBSD measurement in CaF_2 single crystal. It can be clearly seen that based on the dynamic model, the image is the result of the superposition of many waves. The simulations also show that as the result of many wave interferences, we obtain a transverse intensity distribution within the Kikuchi bands (see Fig. 3.19). Compared to background, the intensity of the bands shows a minimum on their border, while it is higher inside the bands. This prediction is in agreement with the experienced intensity conditions during a measurements.

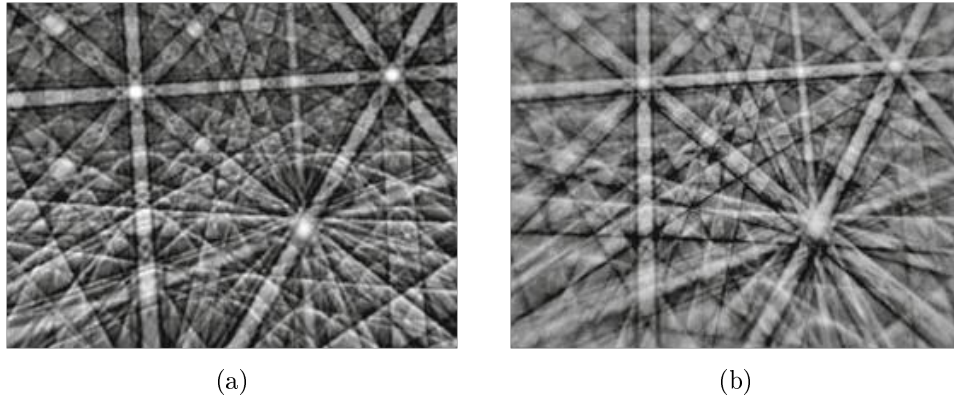


Figure 3.18: *The expected Kikuchi pattern resulted from simulations based on the dynamic model (a) and the real EBSD pattern (b) from a fluorite crystal [16].*

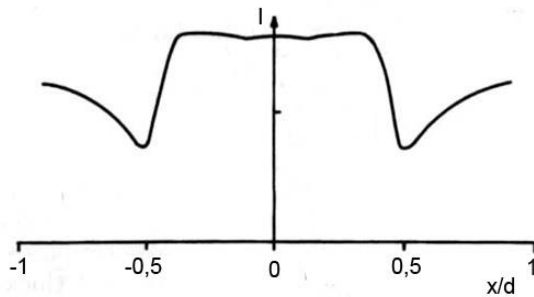


Figure 3.19: *Intensity distribution according to the simulations based on the dynamic model [15].*

3.2.2 Image processing

As it has been described in a previous subsection, Kikuchi lines are related to the arrangement of the set of diffracting lattice planes, and geometry of the Kikuchi pattern is defined by the given crystal structure. Using fast, computer based, fully automated system for identifying the positions and widths of the bands, it is possible to define the structure and orientation of the crystal. The automated determination of the crystallographic properties consists of two steps. First, the indexing of the Kikuchi pattern takes place, which means the identification of the corresponding lattice planes based on their crystallographic indices. In the second step, one determines the relative position of the bands to an external frame of reference. The main problem with the automatization of this process lied in the difficulties in pattern recognition, because the pattern is not merely a set of sharp and straight lines without background, but it consists of bands with low-contrast and non-uniform

intensity distribution together with a noisy high background. There were numerous attempts, e.g., by shape filter method [17], local maxima searching [18], local intensity gradient method [19], but in practice these methods were not so successful as the easier and faster *Radon transform* [20] and *Hough transform* [21]. The Hough transform converts the pattern lines into points (the treatment of the latter is more appropriate for a computer).

There are the diffraction pattern is in an (x, y) coordinate system which origin is in the middle of the image. During the algorithm, the lines in the Kikuchi pattern are transformed by the following formula:

$$\rho = x_i \cdot \cos \theta + y_i \cdot \sin \theta, \quad (3.6)$$

where $\rho \in (-R, R)$ is the distance of the line from the origin and R is the radius of the circle inside which we consider the image (Fig. 3.21); x_i and y_i are points on the original image; $\theta \in (0^\circ, 180^\circ)$ is the angle between the x axis and the normal from the origin to the given line. As it shown in Fig. 3.20, that the lines of the original image are transformed into the so-called *Hough space*, in which we obtain sinusoidal curves defined by (ρ, θ) coordinates. The curves (Fig. 3.20b) represent the set of those lines which intersect each other at the given points (Fig. 3.20a). Therefore, each line in the original space can be described as one point in the Hough space.

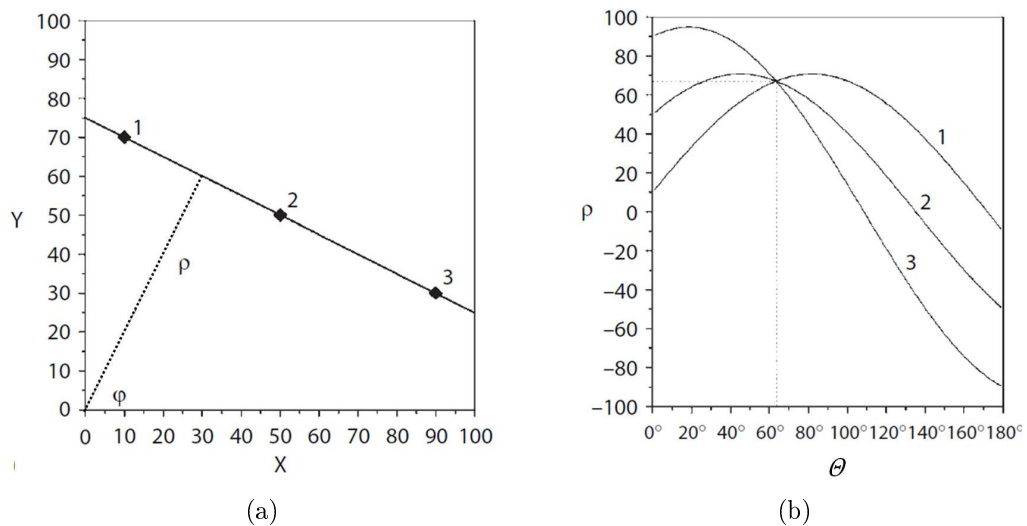


Figure 3.20: A line in the original space (a) and its corresponding point in the Hough space (b) [22].

In case of the EBSD, where the obtained pattern image is gray-toned, it is

necessary to take the intensity of the bands into consideration. Each pixel on the original image has an intensity value that is denoted by $I(x, y)$. All of the pixel intensity values of a line are summed up and added to the value of the pixels in the Hough space $I(\rho, \theta)$. Thus, the intensity of the transformed pixels is given by

$$I(\rho, \theta) = \sum_i I(x_i, y_i), \quad (3.7)$$

where i goes through all points of a line in the (x, y) space. This is the so-called *gray-tone weighted Hough transform*. With the help of this process, we can associate

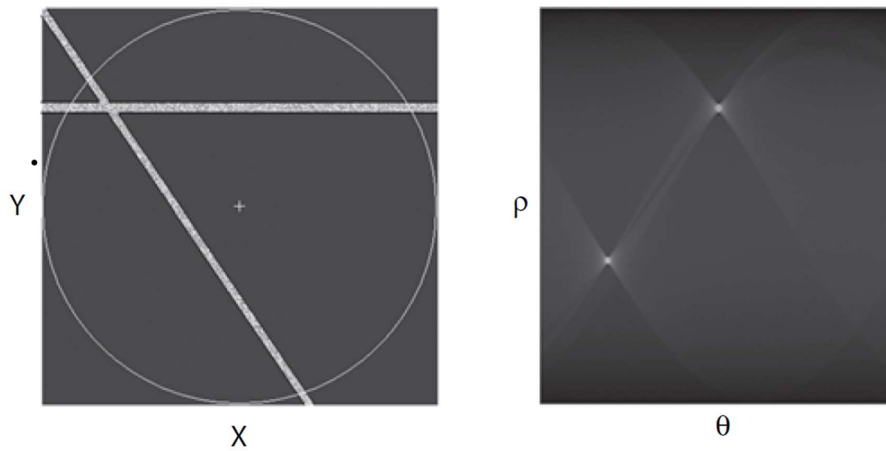


Figure 3.21: *The original image (considered along a circle) and its gray-tone weighted Hough transformed image [22].*

the points with the lines not only by of the coordinates, but also by the intensities (Fig. 3.21).

Generally, the EBSD image processing starts with the subtraction of the background, which starts with capturing an integrated image by the Hikari camera from a relatively large area of the sample surface. The system subtracts the so obtained average background from each pattern, thereby improving sharpness, contrast and quality of the Kikuchi patterns after an amplification. At this point, the type of the crystal structure and the components of the investigated material is set manually. If we do not have previous knowledge about these parameters, we have the opportunity to analyze the sample by measuring the energy of its emitted characteristic X-rays. The next step is the pattern transformation by the Hough transformation, that is followed by the identification of the resulting points in the Hough space. Obviously, it is equivalent with the identification of the bands in the original space.

In the mathematically ideal case, the result of the transform should be one single bright point, which would originate from a bright line of a width of one pixel. The processing of these bright points would be very easy using peak location methods. However, the bands have a width of more than one pixel and a finite extent, thus the result differs from that of the theoretical. Instead of single bright points, we obtain butterfly-like shaped peaks with local extent, therefore the computer uses the so-called *butterfly filter* method for the processing of the non-ideal peaks. The computer selects the brightest peaks, which are suitable for further, more accurate calculations on the original position of the bands. This means that by indexing these bands, we receive information about the orientation of the crystal of which the pattern was recorded. An example is shown in Fig. 3.22.

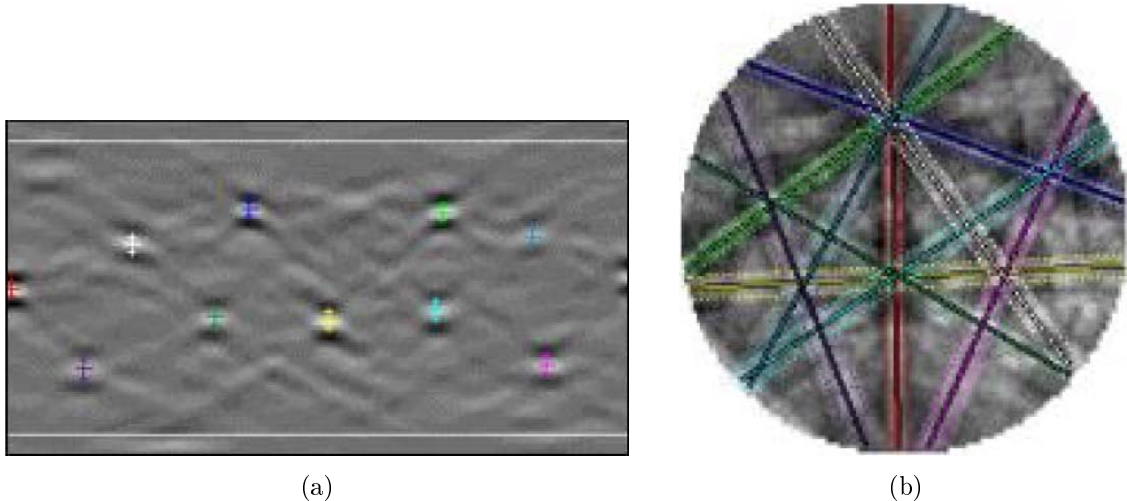


Figure 3.22: *The butterfly shape peaks (a) of the original pattern (b).*

During the indexing step, the computer compares band with measurements and theoretical computations by comparing the corresponding *d-spacing* of the reflecting plane (or d_{hkl}). The aim of the method is to find the most probable reflecting plane that corresponds to the measurements. More precisely, during the calculation, the PC measures the angle between the bands and then compares it with the theoretical interplanar angles from a look-up table [23].

During this, the computer considers all possible sets of three bands which can be formed by the detected Kikuchi pattern, starting with the most intensive bands (we can adjust the number of the sets). Based on the predefined crystal structure, the computer generates all possible three band sets. After constructing all possible sets,

the next step is the comparison of two data sets (theoretical triplets from the table and the experimental triplets). The final triplet is obtained by voting process, i.e., each matching set gets one vote and the computer choose the one with the largest number of votes. The voting table is shown in Fig. 3.23.

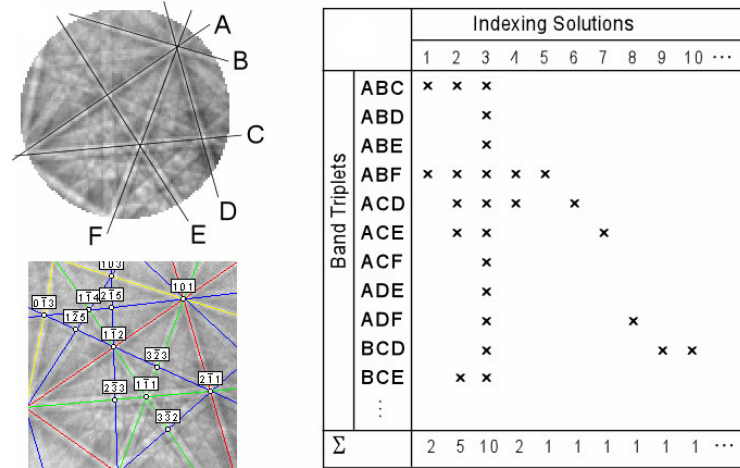


Figure 3.23: The voting table [23].

After the voting method, we can check the confidence of the indexing by the so-called *confidence index* or *CI*. The value of *CI* is given by the following form:

$$CI = \frac{V_1 - V_2}{V_i}, \quad (3.8)$$

where V_1 and V_2 are the number of votes of the first and second best solutions respectively, and V_i is the ideal number of votes, which is equal to the number of all possible triplets. The value of *CI* is between 0 and 1.

3.2.3 Applications of EBSD

In modern a scanning electron microscopes, during the EBSD measurements, high speed and automatic point-by-point orientation determination is performed on the sample surface. The equipment measures the Kikuchi pattern that belongs to the given volume element with a pre-defined resolution and carries out the indexing of the bands. The measurement step size is determined by the previously estimated grain size and by the nature of the actual measurement. For example, in case of high precision measurement of small grains, it is necessary to work with a step distance down to 30 nm. The data related to the orientation of the measured volume element

is stored in the memory of the computer. This information is suitable for making the OM of the scanned sample surface area. Making an OM has several benefits and applications that are the following:

- Representation of texture components as a function of (x, y) position by *inverse pole figure* (IPF) mapping.
- Representation of *image quality* (IQ) map of Kikuchi images.
- Displaying the grain orientation by *pole figure*.
- Characterization of grain boundaries by the orientation differences between the grains located on two different sides of the crystallite.
- Phase mapping.
- 3D representation of texture components.

As the above list illustrates, this method has a rather high potential, considering that each method forms an important part of materials research.

Here, a short description will be given about the orientation determination as well as about the mapping by IPF. Finally, a few lines will be devoted to IQ. The definition of orientation can be approached by many ways regarding to various conceptual bases, however, considering the size limitations of this thesis, I will focus only on the *Euler angles*. In order to specify a crystallographic orientation, the determination of corresponding coordinate systems are required first. In materials characterization, at least two independent coordinate systems are required. Generally, we use *Cartesian* coordinate systems: one is related to the whole sample and the other is related to the grain in question. As it is shown in Fig. 3.24, the three axes of sample coordinate system are labeled by *normal direction* (ND), *transverse direction* (TD) and *reference direction* (RD) (*rolling direction* in case when the sample is a rolled sheet). The grain coordinate system is also shown in the figure – more precisely, its cubic unit cell – whose axes are specified by the three lattice directions of the crystal: 001, 010 and 100. Comparing the position of the two coordinate systems are compared to each other and the orientation can be determined. In order to give a complete picture of the orientation, all three sample directions or the Euler angles must be given.

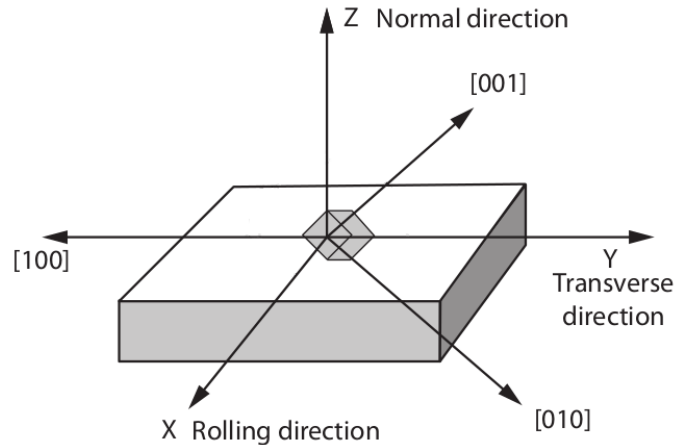


Figure 3.24: *The two required independent coordinate systems for crystal orientation determination [22].*

Since three variables can completely describe the orientation of grains, the three Euler angles are most commonly used. These are three rotation angles and with their help, the sample coordinate system can be transformed onto the single crystal coordinate system. The rotation angles between the sample and the crystal are given as follows (see Fig. 3.25).

1. φ_1 is the rotation angle about the ND axis and it transforms RD to RD'.
2. Φ is the rotation angle about RD' axis that is the transformed axis of RD and this transforms ND to ND' ([001]).
3. φ_2 is the rotation angle about ND' axis and it transforms RD' to [100] direction.

The relation between the sample and the crystallite coordinate system can be defined by successively rotation about the specified axes with the three Euler angles.

The *projection method* gives information about the relationship between lattice planes and directions. There are multiple modes of the projection in crystallography, and all of these are based on the fact that the crystal can be represented by a set of normals corresponding to each crystallographic plane. Consider a sphere with the same origin as the crystal and the extended normals of the planes. In this way we have the setup shown in Figure 3.26, where we can also see the intersections of the normals and the sphere (i.e., the *poles*). The name of this projection technique is *spherical projection*. During another method, i.e., the so-called *stereographical projection*, those poles which intersect the northern hemisphere are projected onto the

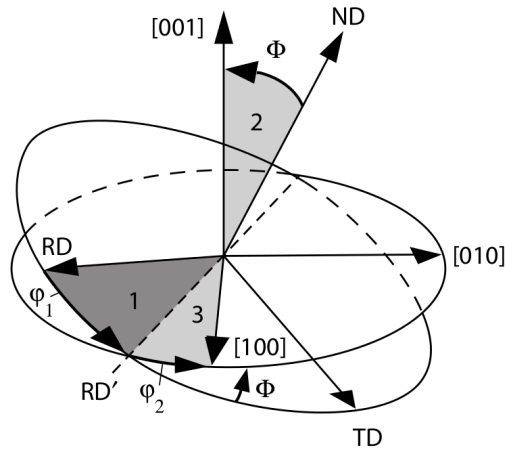


Figure 3.25: *The representation of the three Euler angles [22].*

equatorial plane from the south pole and vice versa. The normals of the symmetric planes are also projected in the first step, and this way in case of a cubic lattice we have 8 equivalent *stereographic unit triangles*.

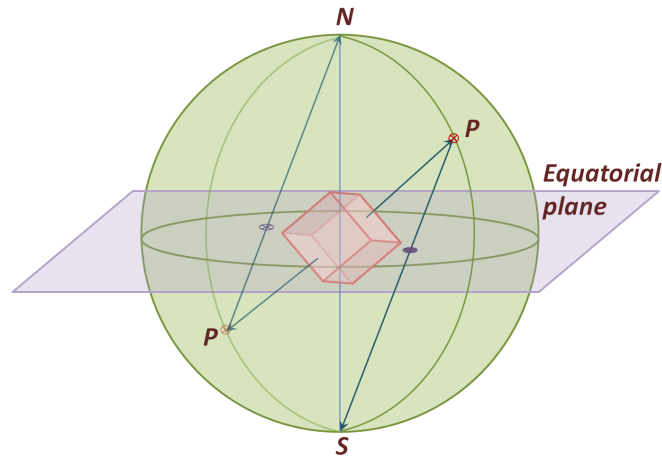


Figure 3.26: *Presentation figure of the spherical and stereographical projections.*

In the pole figure, the projection coordinate system is fixed to the specimen, in contrast to the IPF where it is attached to the crystal. Namely, the latter shows which are the directions in the crystal coordinate system that are parallel to the normal of the sample surface. Different directions are indicated by different colors. An OM as an IPF is shown in Fig. 3.27. In the upper left corner of the figure, section 001, 101, 111 can be seen, in case of a cubic systems. The coloring of the section is used as a reference and helps in the interpretation of grain orientation. Due to its

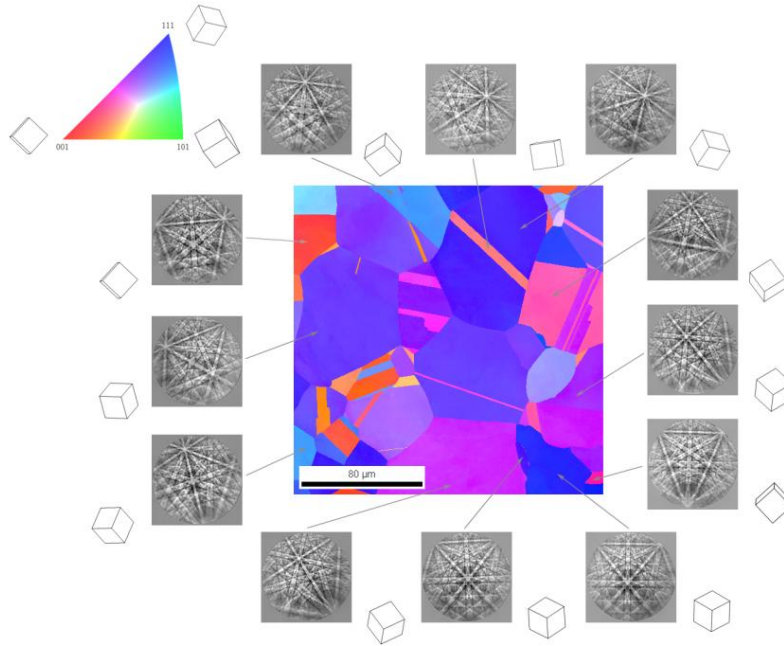


Figure 3.27: *Inverse pole figure of heat treated nickel sample and the Kikuchi pattern of some grains.*

symmetrical properties, only one eighth of the circle is needed for the cubic crystal. It is important to note here that this interpretation by the inverse pole figure is not an unambiguous indication of the grain orientation, because the grain can rotate around the normal direction. Even so, often it is practical to choose this mode of representation, especially when it is known that the texture is circularly symmetric, e.g., in recrystallized or drawn wire samples.

The quality of the Kikuchi patterns can be measured by an *image quality parameter* (IQ), which depends on the material and the measurement conditions, but if we fix the parameters of Hikari camera constant, different measurements can be compared. The value of IQ is given by the sum of the intensity values of peaks which are detected during the Hough transform. IQ map is a gray-scaled image, in which each point corresponds to the pattern quality measured at the same point in the orientation scan. If the diffraction pattern quality is low, the point will be dark, and vice versa. This results in the grain boundaries appearing in IQ with dark color. Due to this strong contrast, the IQ images are also useful during 3D reconstruction, as it will be shown later.

Chapter 4

Results and discussion

4.1 Results

As it has been mentioned before, the FIB tomography, together with EBSD measurements gives useful information about the inner structure and properties of materials. These data can be obtained by other measurements as well, e.g., we can use various products of beam-sample interaction that were described above. Therefore the grain structure can be characterized by using secondary electrons, secondary ions and backscattered electrons (not only by diffraction, but also by imaging). However, these inform us neither about the orientation of grains nor about the nature of the grain boundaries. If we are interested only in the grain size (without its orientation), these measurements give satisfying results in relatively short time.

In the first section of this chapter, I will describe the details of sample preparation and the selection of the sample for the 3D reconstruction. Afterwards, I will describe the experimental and computational parts of the 3D reconstruction method. In the second part, the grain visualization techniques will be described. Finally, I will present the results of the visualization of the EBSD based microstructure characterization by images and movies attached, and the gained statistical data will be presented as well.

4.1.1 Sample preparation

During the work presented in this thesis, my first task was the selection of the suitable sample for the successful 3D volume reconstruction. The aim of these first exploratory measurements was the characterization of the grain structure, the

average grain size, the average number of the nearest neighbor grains to which high quality surface and sample preparation are essential. I carried out the main polishing step using the *SC-1000 SEMPrep* dual Ar ion beam workstation (Fig. 4.1), developed by *Technoorg Linda Ltd.*, Hungary [24], which is suitable for both surface polishing and slope cutting of solid state samples, preparing high-quality surfaces.



Figure 4.1: *The SC-1000 SEMPrep dual beam workstation [24].*

The usual surface treatment techniques (mechanical grinding, multiple steps of polishing) either consume a large amount of energy and time or the process is rather complicated (e.g., electropolishing), and satisfying result can rarely be achieved. Most of the time the sample preparation begins with mechanical grinding and polishing, because the surface to be studied needs to be flat and smooth for EBSD measurements. This mechanical treatment generates a 1 – 100 *nm* thick amorphous layer (the so-called *Beilby layer* [25]) on the sample surface which significantly blurs the diffraction patterns collected by the EBSD detector, since the backscattered electrons come from a shallow subsurface region. This is why the EBSD measurements are very dependent of the surface quality and also the morphology. On the other hand, this feature makes the EBSD a perfect tool for surface quality characterization. In order to remove the amorphous layer one can apply chemical etching or electropolishing, but these methods sometimes coarsen the surface and therefore produce less evaluable results. Because of this a new promising technique has been developed in the last decade. This new method is the ion polishing and milling, the underlying physical phenomenon of which is the atom/cluster sputtering. This

technique uses either low-energy ($0.1 - 2 \text{ keV}$) or relatively high-energy ($2 - 10 \text{ keV}$) ions of inert gases (e.g., Ar^+ , Kr^+ , Xe^+) in a near parallel beam, or some ions of metallic origin, as for instance Ga^+ ones ($2 - 30 \text{ keV}$) in the focused ion beam (FIB) systems. The main benefit of the ion milling techniques is that they are less sensitive to the microstructure and chemical composition of the samples. Other advantages of the inert gas parallel beam technique are the size of the processed area and the low costs of the treatment. While using FIB the size of the achievable area is in the order of $100 \mu\text{m} \times 100 \mu\text{m}$, with parallel noble gas beams one can easily produce a $1000 - 2000 \mu\text{m}$ wide and $100 - 300 \mu\text{m}$ deep polished area. The SC-1000 SEMPrep device is capable of both surface polishing and slope cutting (Fig. 4.2). During the sample preparation, I used only the high energy Ar surface polisher, therefore the further details of the slope cutting will not be presented here.

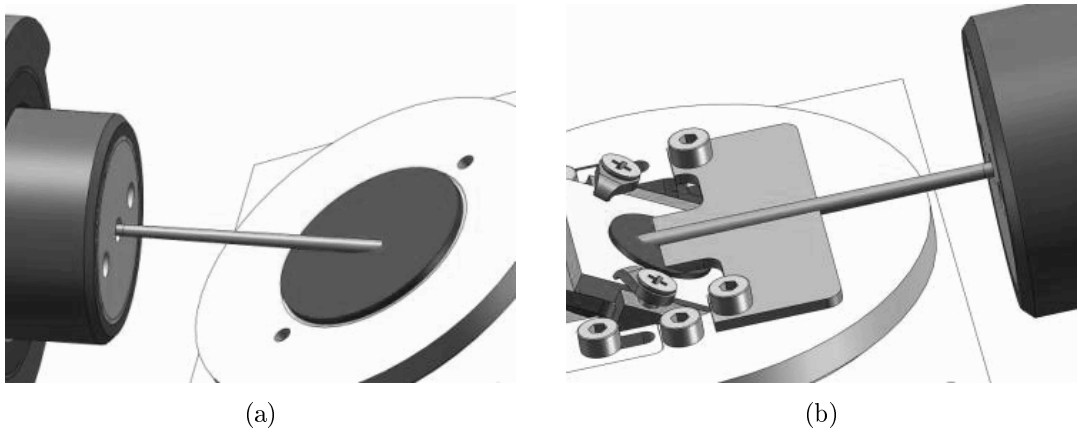


Figure 4.2: *Scheme of the two operating modes of SEMPRep: low-angle surface polishing (a); ion beam slope cutting (b).*

The SEMPRep device was designed specifically for SEM sample preparation. Its stage can be tilted in the range of $0^\circ - 30^\circ$ towards the active ion source with 0.1° precision, and the surface polishing sample holder can do full in-plane rotation or oscillation while using the high-energy ($2 - 10 \text{ keV}$) or the low-energy ($0.1 - 2 \text{ keV}$) ion gun. The size of the ion polished area is set by the stage tilt. The sample is located in a vacuum chamber which holds $\sim 1000 - 600 \text{ Pa}$ base pressure and $\sim 1000 - 400 \text{ Pa}$ dynamical pressure during the ion milling. In papers [26] and [27] we gave a detailed description on the Ar ion polishing of different conductive and non-conductive materials followed by a high-resolution EBSD measurements. In these papers, we demonstrated the advantages of Ar ion polishing and the unique

capabilities of the SC-1000 SEMPrep apparatus and also showed how the optimal parameters of the EBSD-quality surface treatment can be found. All of the presented measurements were started with surface treatment using conventional mechanical grinding and polishing in order to remove the rough bumpiness, and ensure a rather clean, uniform surface to start the Ar ion milling. The EBSD measurements were begun on these samples to determine the initial average of the IQ value. In order to find the optimal ion polishing angle, the angular dependence of IQ was measured. Measurements were accomplished on samples from several different materials (such as Cu Ni, Fe, steel). I will show the results for nickel, since the result was crucial in the present work for finding the suitable sample for reconstruction. As Fig. 4.3 shows in case of nickel, the optimum of the sample tilt during surface polishing using SC-1000 SEMPrep is about 8° and the optimal time is 6 min .

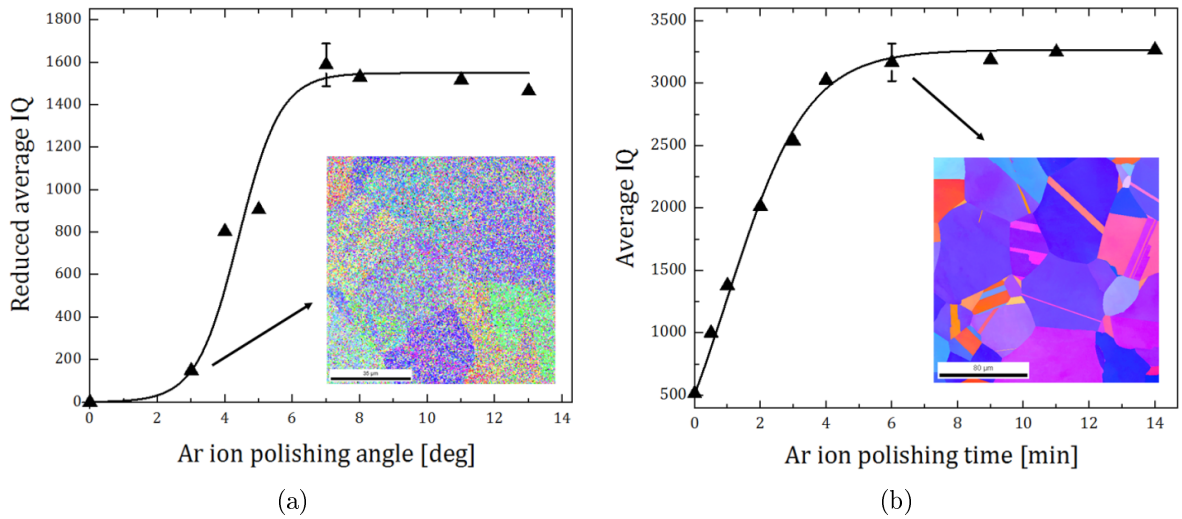


Figure 4.3: *Dependence of the average IQ value on the ion beam incidence angle (a) and on the total time of ion polishing (b), measured on Ni.*

In order to find a suitable sample for the reconstruction, I carried out some previous exploratory EBSD measurements with various Ni samples. Nickel is a medium hardness transition metal that has medium melting point and it is highly deformable. It crystallizes in face centered cubic (fcc) crystal lattice. Nickel is a very important metal and it has various applications, especially as an alloying element. It is usable to increase the hardness of steel alloys and it is also successful in the development of corrosion-resistance of stainless steels. I had four high-purity nickel samples in which the measurements were made: two wires and two rolled sheets

(one annealed and one in as received from each one). The samples were annealed at 700°C for one hour. In total, I made six exploratory measurements, because the wire samples had two different cutting profiles (parallel and perpendicular to their length).

In case of each samples, I made the following preparation steps in order to have high quality EBSD measurements:

1. two minutes grinding with abrasive paper of 1200-grit,
2. one minutes grinding with abrasive paper of 2500-grit,
3. three minutes grinding with abrasive paper of 4000-grit,
4. ten minutes polishing using alumina paste of $1\ \mu\text{m}$ average particle size,
5. twenty minutes polishing using alumina paste of $0.3\ \mu\text{m}$ average particle size,
6. inspection of the surface quality and further thirty minutes polishing with $0.05\ \mu\text{m}$ particle size aluminium oxide paste if it was necessary,
7. six minutes surface polishing using Ar ions by SC-1000 SEMPprep at tilting angle of 8° with sample rotation. The accelerating voltage was $10\ \text{kV}$.

Figures 4.4-4.5 show the OM by IPF of two section planes of the drawn wire and the rolled sheet, respectively. One can see in the figures that there are no sharp, well-defined grain boundaries and the grains cannot be distinguished from each other. Therefore, these samples would not be suitable for a easy and demonstrative grain reconstruction.

In case of the annealed samples, we obtained well-defined grain boundaries, as it is shown in Figures 4.6-4.7. Finally, we have chosen the sheet sample, due to the fact that it contains larger area with smaller grains, and the implementation of the slicing was also easier than that of the wire. Namely, if we prepared the specimen on the edge of the sample holder, the edge of the sheet became free and we were able to tilt it exactly into the direction of the ion source in order to take images with ions. Furthermore, less material is needed to be removed from the specimen. The latter is useful since we could obtain high quality, shadow-free EBSD images and less material sputtered back to the interested area, and it is also faster and less

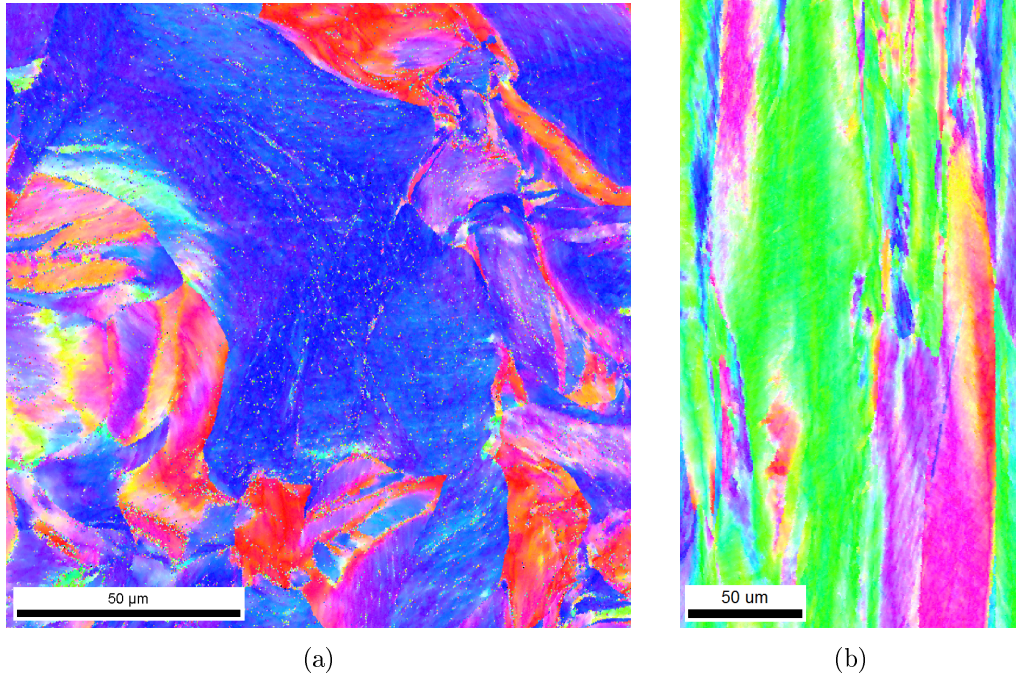
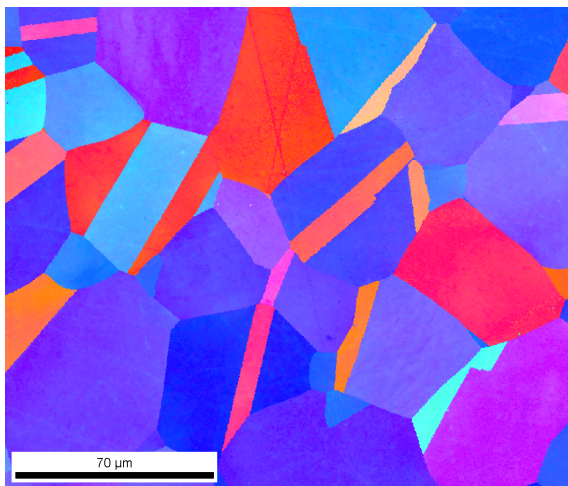


Figure 4.4: *Orientation maps of the perpendicular (a) and parallel (b) cutting planes of the drawn wire sample.*

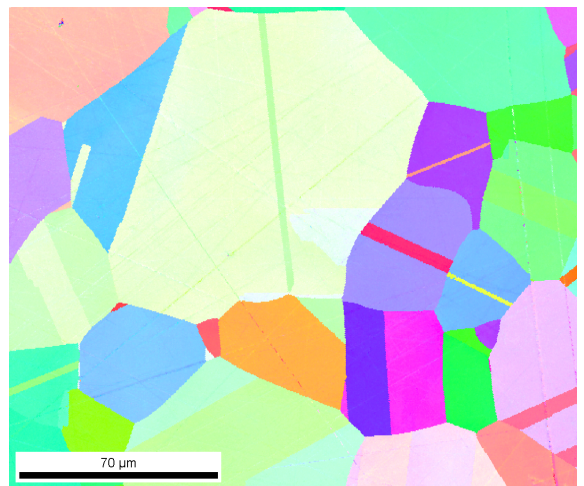
expensive due to the lower Ga consumption. Further details of the experimental steps will be described in the next section.



Figure 4.5: *Orientation map of the rolled Ni sheet.*



(a)



(b)

Figure 4.6: *Orientation maps of the perpendicular (a) and parallel (b) cutting plane of the annealed Ni sample.*

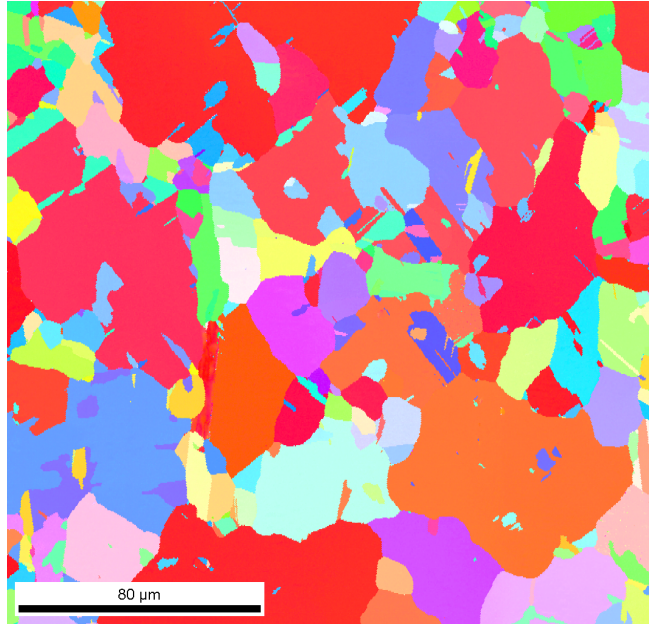


Figure 4.7: *Orientation map of the annealed Ni sheet.*

4.1.2 Three dimensional reconstruction

Due to the development of the scanning microscopy, tomography techniques and computing, nowadays we have the opportunity to measure the 3D grain orientation distribution and to visualize the structure of a given volume using EBSD technique. In general, with this method (together with the orientation determination), we can define further properties of the materials such as the grain's volume, surface area, perimeter length; total number of neighbors; grain boundary character; and its morphology [28, 29, 30]. Additionally, during the investigation of alloys, the technique is suitable for the characterization of different phases (together with the description of their size and distribution), and also for the determination of the microstructure [31]. The analysis of the pore size distribution by the reconstruction of porous materials shows another applications of the three dimensional reconstruction [11]. Based on the above, this technique is useful in both quantitative and qualitative analyses. As it has been mentioned before, FIB tomography is a serial sectional destructive method, during which we slice the cross-sectional surface of the material in several steps by high energy focused ion beam. After each slice, a high resolution EBSD image is made from the newly exposed area of the sample. When the 2D slices are ready, we can begin the 3D process of the images using an appropriate software.

Experimental work

I carried out the complete measurement manually, without any automation. After the selection of the sample, we looked for a suitable area on the sample which is appropriate for further work and for the reconstruction, e.g., an area that contains many small grains. We assumed that the presence of smaller grains on the surface implies the presence of small grains in the inner part of the nickel sheet as well. It was important to have this area on the edge of the sheet in order to simplify sample positioning during the measurements as well as the processing of the ion images. Figure 4.8 shows the selected area in top view. The surface of the sample is slightly contaminated, since I did not performed the grinding and polishing steps on this specimen (the image in Section 4.1.1 was made on an other annealed nickel sheet). Obviously, the sample preparation was not necessary, as we cut the sample perpendicular to its surface and the EBSD measurements was performed on that surface.

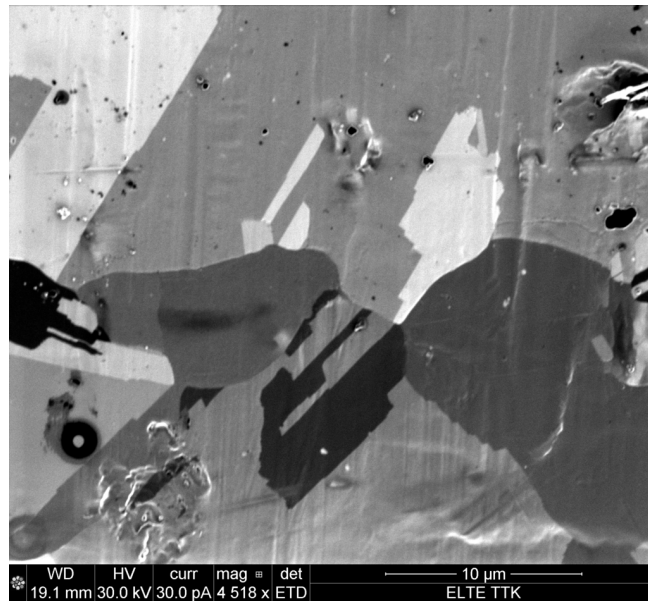


Figure 4.8: *The selected area for reconstruction (top view).*

The next step was the appropriate preparation of the selected area. Our goal, as usual, was a wide cut on the two side of the area for the high quality EBSD measurements (without shadows). We started with the deposition of a protecting platinum layer on the surface in order to avoid the damages of the area of interest during the cutting by FIB. Namely, the ion beam has a finite extension (the so-called

halo), thus it can etch into the area in question without the protecting platinum layer. Figure 4.9 shows the selected surface coated by Pt. During the coating process, we use the built-in gas injection system that is a Pt reservoir with a thin needle end. First, we heat the platinum, then we insert the needle to the sample chamber and open it. Then, we turn on the ion beam with relatively low current density, in which case the ions are depositing the Pt on the sample surface rather than milling into it. The coated area was $33\ \mu\text{m} \times 33\ \mu\text{m}$ with layer thickness of $2\ \mu\text{m}$, the ion beam current and the accelerating voltage were $0.5\ \text{nA}$ and $30\ \text{kV}$, respectively.

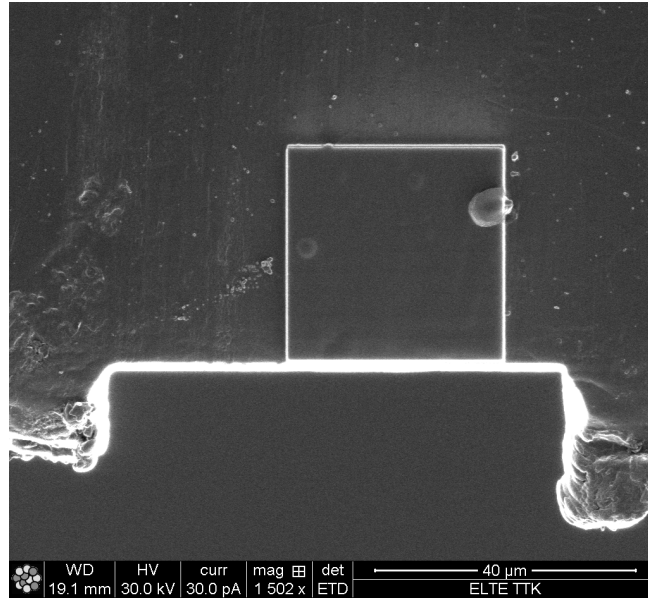


Figure 4.9: *The protecting platinum coating on the surface of the area of interest.*

After Pt deposition, we cut into the Ni sheet through several cross-section steps. The final setup is shown in Figure 4.10. As it can be seen, we etched markers with the purpose of accurate adjustment of the same position on the sample during the different measuring steps. Furthermore, during the further computer based reconstructions it was crucial that successive two dimensional images do not be shifted relative to each other, therefore we had to carry out high precision image adjusting.

The adjusting markers were also applied in the case of the EBSD measurements. The positioning of the reference markers was rather difficult, due to the fact that the surface of the measured area was always varying, and we could not locate by

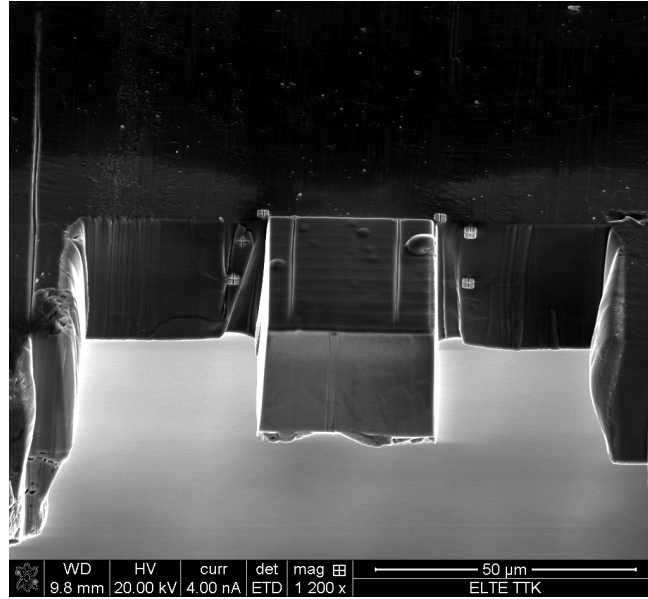


Figure 4.10: *Result of the preparation work.*

the markers near the working area. Thus, we etched two V-shaped markers into the Pt coating (as it is also shown in Fig. 4.10) expecting two sharp traces on the OMs. Unfortunately, these markers did not provide the desired result, since they were not sharp enough and they had not well-defined shape in the IPF images, or in some cases they did not appear in the OM. After all, we defined a square on the screen with given coordinates and we adjusted its bottom edge to the borderline of Pt and the sample before all EBSD scan, as illustrated in Fig. 4.11. We obtained better results by this technique, although during the reconstruction, several manual corrections were necessary due to the small imperfections of the adjustment, e.g., a low degree of rotation and shifting (in the order of magnitude of tenth of a micrometer) between the images.

After these preparation steps we started the serial sectioning work with FIB. We made 60 slices in total. Considering the stage movements between the slicing and the EBSD scan, together with the adjustments, we managed to process 1 slice per 1.5 hour. This part of the work consists of the following main steps.

1. *Slicing*

The previously presented exploratory measurements from the annealed nickel sheet showed that the expected size of the smallest object in one direction is around $5 \mu\text{m}$. In order to create a good quality three dimensional reconstruc-

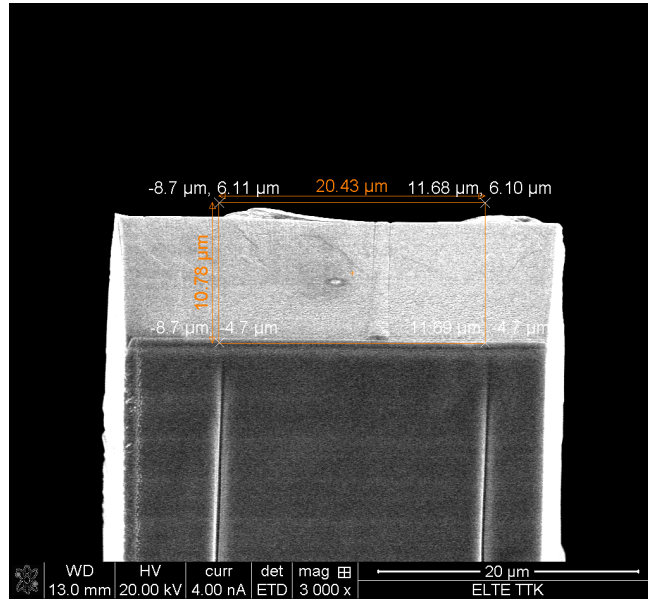


Figure 4.11: *The adjusting step before the EBSD measurements.*

tion, the number of slices from the smallest grain should be at least 10, thus the thickness of the slices was set to $0.5 \mu m$. During the milling, the value of the ion beam current was $3 nA$, the accelerating voltage was $30 kV$ and the milling depth was $8 \mu m$. This part of the process took about 11 minutes for each slice. The sample was tilted by 52° , so that the FIB was able to cut perpendicular to the surface.

2. *Top view snapshot*

We took a top view snapshot after each slice in order to check the real size of the cut area. I made a video to illustrate the change in the length of the chosen area of the specimen. This video is available on the CD attached to the thesis and also on my webpage [32].

3. *High resolution EBSD measurement*

We rotated and tilted the sample to the right position for the measurement by the Hikari camera. At each day, before the first EBSD measurement, we recorded the average background with the same parameters and subtracted it from all Kikuchi patterns during the scans. Before every EBSD measurement, we checked the rotating position of the sample by the help of markers which provided the same orientation of the analyzed area in the different measurements. Then we used the above mentioned adjusting square for further

positioning the specimen. The parameters of the EBSD measurements were the following: 20 kV accelerating voltage, 4 nA electron beam current and the size of the measured area was $34\ \mu\text{m} \times 37\ \mu\text{m}$ with $0.1\ \mu\text{m}$ scan steps. One scan took about 44 minutes.

4. *Snapshot from the measured area*

After each EBSD scan, we took an image of the surface of the new area (using the ion beam excited secondary electrons) in order to illustrate further opportunities of reconstruction by ion images. These will be presented in the next chapter.

Computational work

The processing of 2D slices was carried out by the help of the *Amira 5.2.2* software which is a 3D data visualization, analysis and modelling program. Amira is useful in various scientific fields, e.g., medicine, biology, biochemistry, microscopy, etc.

The set of the 2D slices is called the *image stack*, which is the basis of the 3D reconstruction. An illustration of the image stack, which is built up by some selected OMs, is shown in Fig. 4.12. The resolution of the reconstruction depends on the

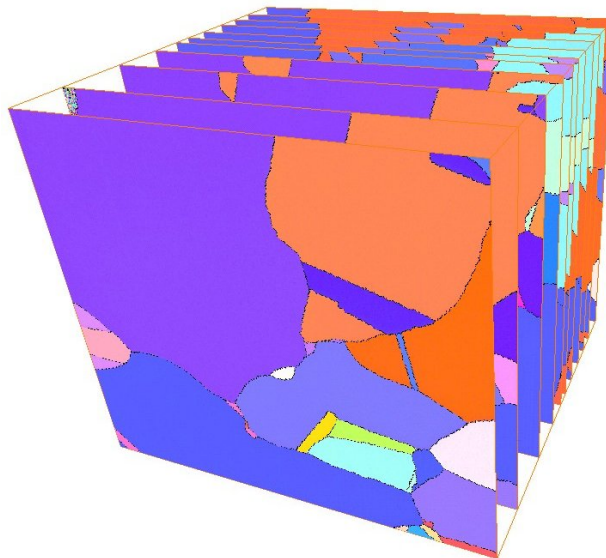


Figure 4.12: *Illustration of the image stack which built up from 2D orientation maps selected by myself.*

predefined slice thickness and generally it is the lowest in the z direction (or slicing

direction).

In the following, several useful basic terms related to tomography will be introduced. The smallest unit of a digital 2D image is the *pixel*, which is the face of the "three-dimensional pixel", the so-called *voxel*. A voxel is a 3D volume element, and it is the other important basic unit of the visualization, due to the fact that the sum of these voxels constitutes the entire volume. The size of the voxel is given by the simple expression:

$$VV = \frac{FOV_x}{matrix_x} \times \frac{FOV_y}{matrix_y} \times ST, \quad (4.1)$$

where VV denotes the volume of the voxel; FOV is the field of view, which is the size of the reconstructed area in the x and y direction, respectively; $matrix$ is the number of pixels ($rows \times columns$); and ST is the slice thickness. The unit of voxel volume is given by the unit of the field of view times the unit of slice thickness.

During the computational 3D reconstruction, I used the images made by ions and also the images received from the EBSD measurements. More precisely, I used the IQ images, since they have higher gray value differences than the maps by IPF (Fig. 4.13), which has many advantages, as we will see in the detailed description of image segmentation. Furthermore, Amira is able to handle only grayscale images during the segmentation process, thus the color code information linked to the IPF images is lost. Nevertheless, the orientation information was available from the OMs and I could assign the corresponding colors to the individual grains.

The steps of 3D reconstruction using Amira were the following.

1. *Importing of 2D pictures*

Although this step sounds rather simple, it is worth mentioning that the definition of the voxel size has to be set at this step. The OM (and also the IQ) images were made from a $34 \mu m \times 37 \mu m$ area, the matrix was $942 pixel \times 1024 pixel$ large and the slice thickness was $0.5 \mu m$. Therefore, the voxel size was $36.09 nm \times 36.13 nm \times 500 nm$ in case of the OM and IQ images.

2. *Slice alignment*

The precise alignment of the slices is a key step as it determines the quality of the final reconstructed volume. Amira offers automatic and manual options

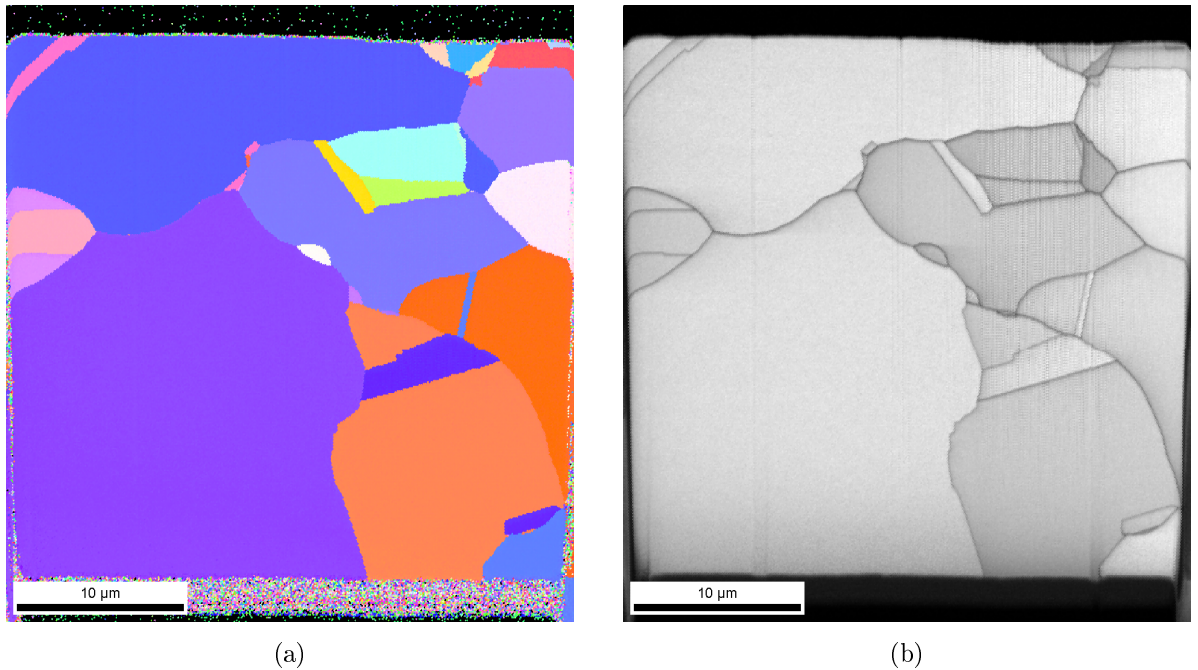


Figure 4.13: *The orientation map (a) and the image quality figure (b) of one slice of the chosen annealed nickel sample.*

with various modes in each case. After the images were imported, despite our previous efforts, I observed some inaccuracies such as displacements and small rotation between several slices. Unfortunately, due to the complex and varying shape of the grains, the faster and easier automatic alignment was not a feasible option. I adjusted a few of the slices manually by the using landmarks (a type of reference point) and the rather interactive basic manual alignment mode. In the basic manual alignment mode one has the possibility to align consecutive slices in pairs, although it is a slow and less accurate mode. If the slices are aligned, further adjustments can be performed by monitoring the value of the so-called *quality function*. There is an automatic optimization calculation of the quality function which is based on the differences between the squared gray value of the current slice pair. The value of the quality function is between 0 (for low quality adjustment) and 100 (for high quality adjustment), and the method is dedicated to maximize its value. To image pairs, for which the grain structural changes were not significant, I could use this automatic option.

3. *Image segmentation and labeling*

Image segmentation is a separation process that helps in the identification of different grains in the 3D image stack. During image segmentation, I assigned each pixel and also determined to which grain the given pixel belongs. I have created a so-called *label field* in which I defined labels for different orientations of the grains. Each label was named by its Euler angles and I assigned the corresponding color from the OM images to it. Thus the important information that the IPF provides is also included to the 3D representation without any loss. Amira offers automatic and manual segmentation methods. Automatic methods are based on the grey values of the image pixels and on the region or edge detection. These can be used for images that have large differences in the grey values. For example, the threshold operation compares the pixels' grey value with a user-defined threshold and the pixels that have grey value in the range of the threshold are selected. The edge detection method compares the difference in the grey values of two neighboring pixels. If it detects significant difference, it assigns the pixels as being part of different objects.

Another semi-automatic segmentation is the interpolation between two assigned slices. The objects in the intermediate images are automatically segmented. Unfortunately, this is not able to process complicated structures such as grains with varying shapes. Therefore, I have performed the image segmentation manually which resulted in a relatively slow and time consuming progress. Thus, the results I obtained were more precise, which is a prerequisite for the surface generation and accurate volume measurements. For the assignment of the pixels, I used several selection tools that might be familiar from other image manipulation programs, e.g., blow tool, brush, lasso select, magic wand, etc. Blow tool is a relatively fast tool and it works with a low level of error. It is a region growing algorithm that begins at a chosen pixel and selects those connected pixels that have grey value within the given tolerance interval. The growth stops when it reaches the edge of the actual structure, as the result of an abrupt (and large) change in the pixels grey value. We can increase the value of the threshold of tolerance, which moderates the stop of the growing contour and sets the difference in grey value which is still accepted.

4. *Interpolation between slices*

The resolution of the reconstruction in the z direction (which affects the voxel

size) is one order of magnitude lower than the resolution in the x and y directions, since the slice thickness is much greater than the measured area by EBSD. This results in stair-case effects in the data sets. In order to avoid these undesirable effects, interpolation between the labels is carried out. With this module, we are able to add intermediate virtual slices in the label field using an appropriate interpolation method. We can set the number of intermediate slices, i.e., the virtual resolution in the z direction.

I have tested this module with several number of intermediate slices and the optimal number turned out to be nine, as a result of balancing between high spatial resolution and still be able to effectively process the labels in the further steps. This process produces 591 slices in total, thus the final slice thickness after interpolation was 50 nm . There are two interpolation types, linear and cubic. The linear interpolation is a simple method that uses linear function and it only draws a line between the two measured data points. The cubic interpolation is a more sophisticated method that considers more than two points during the curve fitting between two points and it causes real continuity between the points. Therefore, I applied cubic interpolation instead of the linear one, and it gave smoother results. To illustrate the effect of the number of extra slices on the reconstruction, Fig. 4.14 shows a grain at different slice numbers (before the smoothing process).

5. *Surface generation*

When the 3D volume is segmented, the software is able to generate a topologically correct polygonal surface model without self-intersections and gaps. The surface generation module calculates triangular approximation of interfaces between different labels. The generated surfaces can be described by a list of triangles and their three dimensional coordinates (i.e., each grain is represented by a corresponding triangle mesh). The surface must be consistent with the labeling, that is, the separated surfaces should be distinguishable and contain no overlaps. Other requirements refer to the shape of the generated surface, e.g., it should be smooth. Depending on the resolution of the label field, the generated surface might contain increasingly large amount of triangles, that can cause a slow-down in further treatment of the surface.

6. *Surface editing and smoothing*

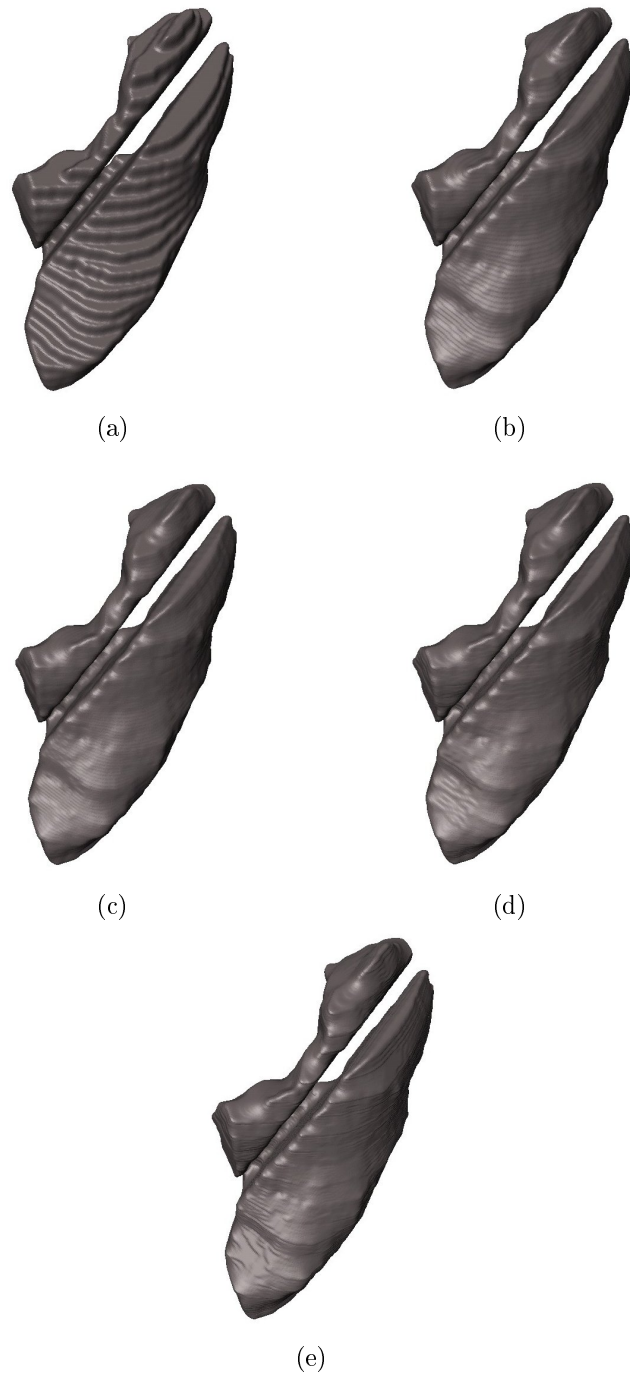


Figure 4.14: *The comparison of the results with different intermediate slice number: row data (a), three extra slices (b), five extra slices (c), nine (d) and thirteen (e) intermediate slices.*

If it is necessary (e.g., the generated surface still contains an undesired level of roughness), we can apply further editing (e.g., triangle addition or removal,

edge flips) and smoothing algorithms. The smoothing module shifts the vertices of the surface, so that each vertex is translated towards the average position of its neighbors. Face refining method gives a spectacular result, by bisecting the edge of each triangle, and thus replacing them by four smaller triangles. After this step we can repeatedly test the surface, such as by intersection test, closedness test, holes test.

7. *Surface simplification*

During the simplification step, we are able to reduce the number of triangles with a chosen value by an edge collapsing algorithm. This step is essential from the aspect of further work, due to the fact that the larger the number of visualization triangles is, the more time-consuming the interaction with the reconstructed object becomes. However, it is important to consider that this method reduces the quality of the reconstruction, therefore we have to find an optimal value for the number of triangles at which the surface preserves its shape and good quality.

8. *Image cropping*

After the steps listed above, I cropped out the interesting part of the volume. By doing this, the reconstructed volume is reduced by a few μm^3 . Finally, after all post processes described above, the effective part of the measured volume is $31.2 \mu\text{m} \times 29.2 \mu\text{m} \times 27.9 \mu\text{m}$.

Reconstruction results

Three dimensional reconstruction is possible using non-EBSD based FIB tomography, due to the fact that the information given by the interaction between the beam and the sample also reveals the character of the microstructure.

The first option is the detection of secondary electrons excited by the incoming electron beam. In this case we are able to see the grain orientation contrast due to the dependence of SE emission on the on the single crystal orientation of the grains. Figure 4.15 shows this effect. One can see higher and lower intensity areas mapping out the grains with different orientation. Due to this effect, we have the opportunity to visualize the selected volume without time-consuming EBSD measurements.

The second option for a fast and effective reconstruction is the usage of secondary

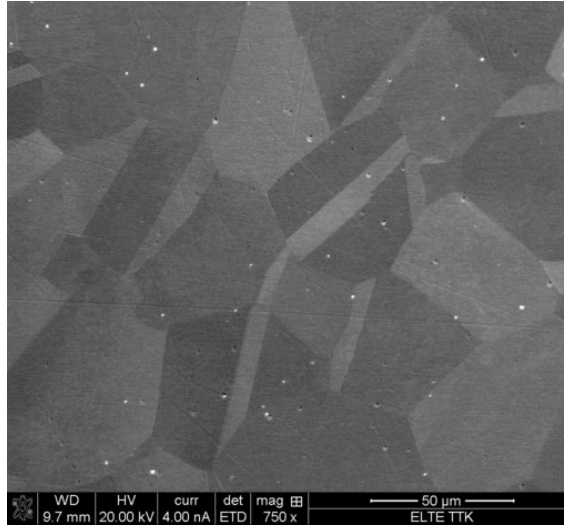


Figure 4.15: *Secondary electron images of heat treated nickel wire. The grains are visible based on the fact that areas with different orientation emit different amount of secondary electrons.*

electrons excited by the ion beam. The phenomenon on which it is based is the *channeling effect* that takes place during the interaction between ion beam and the specimen. In order to illustrate this effect, a few ion excited SE images are shown in Fig. 4.16. These images were recorded from the same area at different tilt angles.

The background of the effect is the penetration depth of ion beam, since ions with same energy can penetrate greater or lower distance depending on the orientation of the polycrystalline sample at the given point. If the sample has a region with low index direction, the penetration depth of the ions is higher, and therefore it will produce SEs deep in the sample. At this depth the electrons has an energy not enough for escaping out of the sample and this area will appear darker. Conversely, if the ions hit areas with high index directions, this single crystal region will be brighter as ions can not penetrate depth enough and many SEs will be detected. Due to this varying yield of SEs, we see rather high contrast differences on the surface, and thus areas with different orientation (that is, grains of the micro- or nanostructure) become visible. Obviously, if the sample tilt is changing, the angle of the atomic layers relatively to the beam direction is also changing. This is the short explanation for the varying contrast of same areas during sample tilting in Fig. 4.16.

During the slicing process, I made ion excited SE images from all 60 slices. In

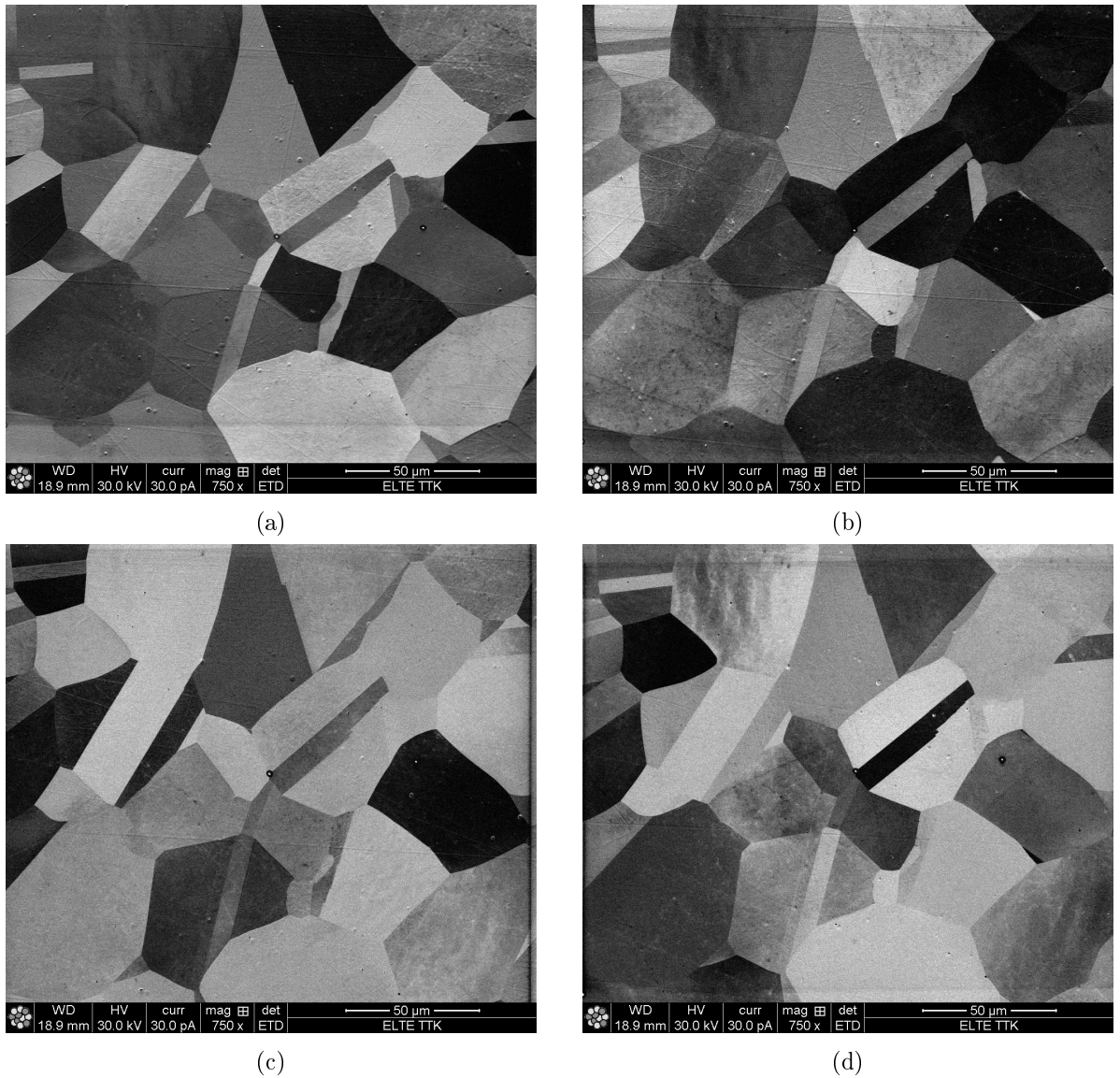


Figure 4.16: *The presentation of channeling effect by ion excited secondary electron images. The sample tilting degrees are 15° (a), 25° (b), 45° (c) and 74° (d).*

all images, the grains with different orientation were well recognizable. In order to visualize it, I made a short movie (using these images with Amira), which shows that we could characterize the grain structure in the entire volume (Video 4.1). This video can be found on the attached CD or on my website [32] with name *ion images*. I have also made an extracted grain from these electron images (Fig. 4.17) and also a short movie (Video 4.2) (written on the CD and it can be also found on my webpage). The grain shown in figure has a volume size of $355.16 \mu\text{m}^3$.

The third option is the utilization of the orientation contrast of the backscattered

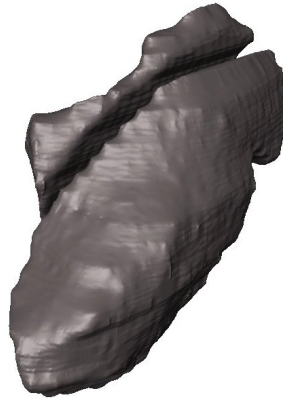


Figure 4.17: *Reconstructed grain using ion excited secondary electron detection. In this case the information about the grain orientation is missing.*

electron images (excited by the primary electron beam). The basis of this is the channeling effect as in the case of the ions. When the electron beam is moving along a direction with lower atomic density in the crystal, it can penetrate deeper before scattering, than in the case of denser atomic directions. In the first case, the probability that the backscattered electrons can reach the detector is less and this will result in lower intensity on the monitor. However, the differences in the backscattered electron yield is much less, than in case of ion excited secondary electrons. This is why, in this case, it is necessary to use an extreme amplification of the contrast (Fig. 4.18).

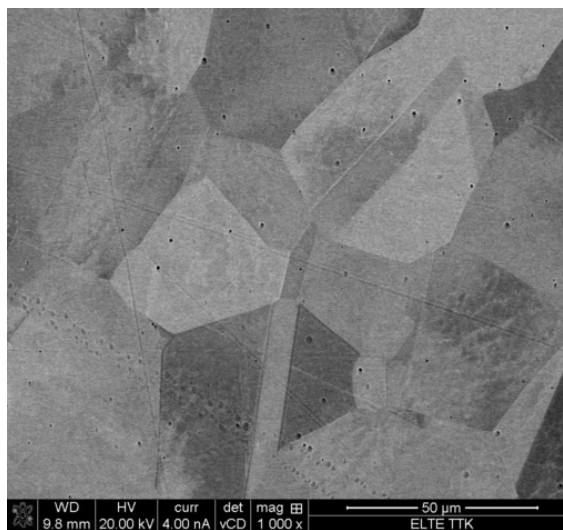


Figure 4.18: *Image showing the orientation contrast using backscattered electrons.*

As it was described, the 3D EBSD reconstruction of the entire volume was made by using both IQ and OM images. After the image cropping, the final effective size of the reconstructed volume was $31.2\ \mu\text{m} \times 29.2\ \mu\text{m} \times 27.9\ \mu\text{m}$. This cube together with the scale bar can be seen in Fig. 4.19 or Video 4.3, the surface of the Ni sample is in the x-z direction.

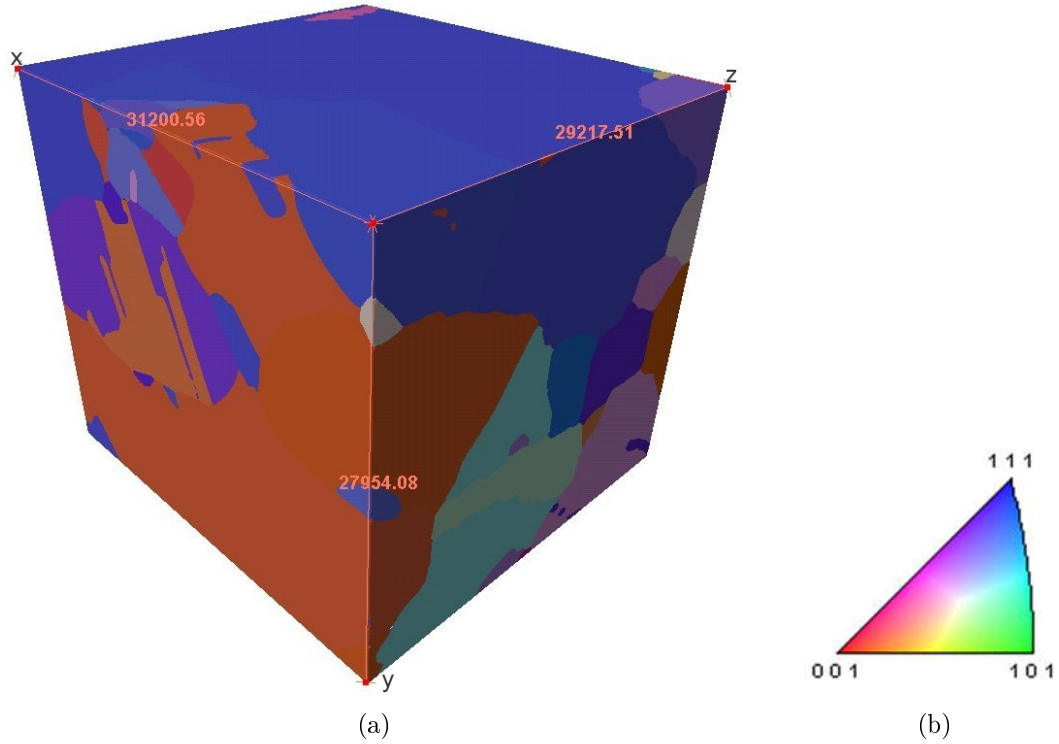


Figure 4.19: *The final volume (a) with the reference triangle (b). The axis values are given in the units of nanometers.*

The volume contains 85 different grains in total, of which 13 are whole grains. One of the full grains will be not presented in this thesis, as the size of this grain is very low ($< 1\ \mu\text{m}^3$ volume) and its shape was thin and elongated. Therefore, the reconstruction of the grain was not accurate enough.

In the following, I will show the other twelve entire 3D grains by images and attached videos, and I will present the received quantitative data by statistical evaluation. All short videos can be found on my website [32] using the same number as here.

The grains together are shown in Fig. 4.20 and on Video 4.4.

Table 4.1 shows the information about these grains, such as orientation, volume, surface area, number of the first neighbors, figure and video number.

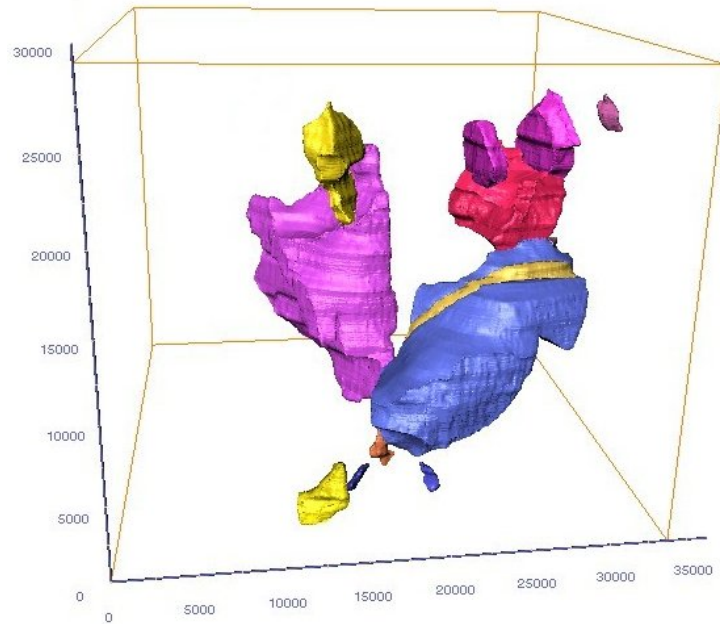


Figure 4.20: All of the 12 whole grains. The scale values are given in nanometers.

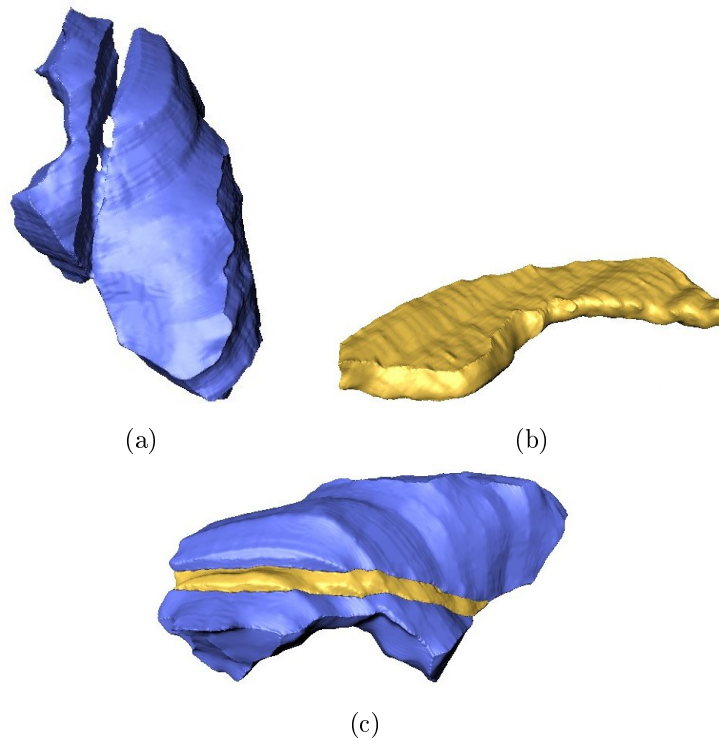


Figure 4.21: The grains with 325, 114, 231 (a) and 306, 70, 268 (b) Euler angle and together (c). The video 4.18 shows the grains together.

Orientation (Euler angles)	Volume (μm^3)	Surface area (μm^2)	Nearest neighbors	Figure	Video
325°, 114°, 231°	355.16	436.88	17	4.21a	4.5
306°, 70°, 268°	30.82	100.93	4	4.21b	4.6
272°, 109°, 247°	321.71	418.34	8	4.22	4.7
114°, 85°, 4°	157.17	183.52	11	4.23	4.8
291°, 74°, 19°	31.69	70.82	7	4.24a	4.9
291°, 74°, 19°	16.77	44.94	6	4.24b	4.10
80°, 160°, 270°	33.11	73.89	5	4.25	4.11
154°, 90°, 159°	4.45	21.95	4	4.26	4.12
88°, 81°, 339°	1.40	7.58	3	4.27	4.13
76°, 167°, 11°	1.23	8.40	5	4.28	4.14
82°, 103°, 340°	0.83	6.58	2	4.29a	4.15
159°, 133°, 39°	0.54	4.96	3	4.29b	4.16
159°, 133°, 39°	0.41	3.99	3	4.29c	4.17

Table 4.1: Data of the whole grains.



Figure 4.22: *The 272, 109, 247 oriented grain.*

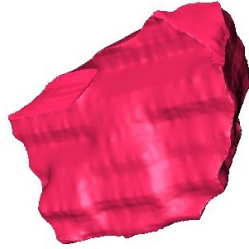


Figure 4.23: *Grain with Euler angles of 114, 85, 4.*

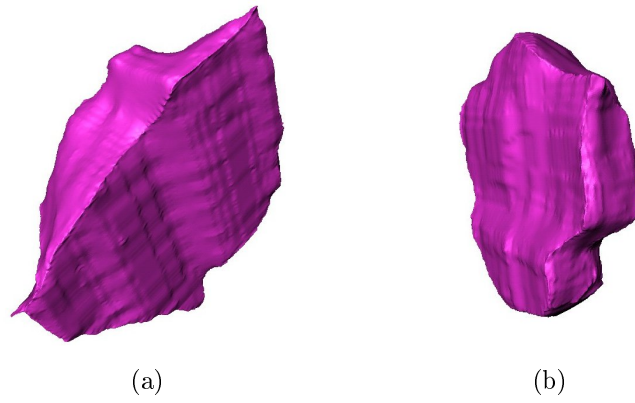


Figure 4.24: *The larger (a) and smaller (b) grains with Euler angles of 291, 74, 19.*

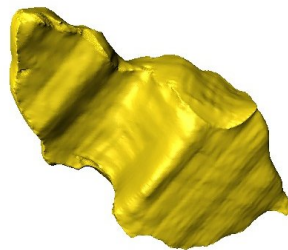


Figure 4.25: *Grain with Euler angles of 80, 160, 270.*



Figure 4.26: *Particle with Euler angles of 154, 90, 159.*

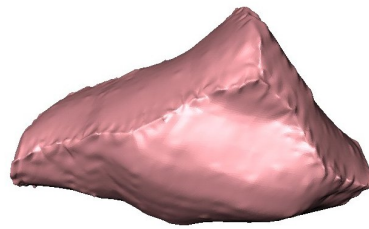


Figure 4.27: *Particle which has 88, 81, 339 orientation.*

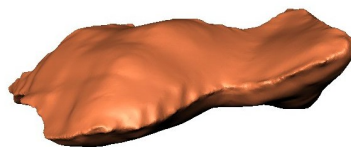


Figure 4.28: *The grain orientation of this particle is 76, 167, 11.*

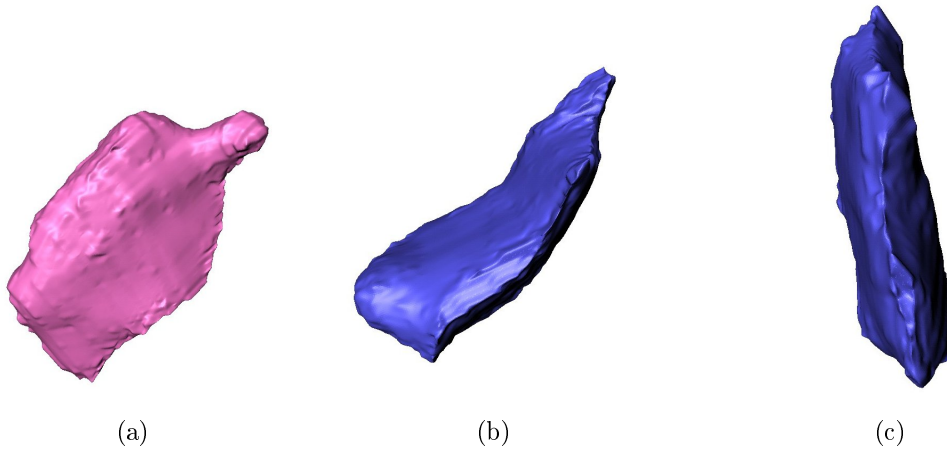


Figure 4.29: *The smallest reconstructed grains with 82, 103, 340 (a) and 159, 133, 39 (b, c) orientations.*

4.2 Discussion

In this thesis, it has been presented the technique of microstructure characterization with EBSD based FIB tomography using the FEI Quanta 3D SEM-FIB system. The mapping of the 3D inner structure of materials using FIB with EBSD has become available in the last decade. Prior to this it was possible to obtain information from the texture only in 2D by EBSD measurements.

I have reviewed the physical background of both SEM-FIB and EBSD systems and I have shown the main steps of material reconstruction. As we have seen, EBSD is a surface sensitive material investigation technique that gives information not only about the size and 2D extension of the grains, but also about the orientation of those, that is the texture of the sample. In order to find the appropriate sample for successful 3D grain visualization, I prepared the surface of the possible specimens with SC-100 SEMP rep equipment. After the selection of the sample, we sectioned it serially with pre-defined steps, and after each slice we made an EBSD measurement and also an image by ions. Finally, I created the 3D reconstruction of the volume by Amira 5.2.2 software in several steps.

As we have seen above, after an effective serial sectioning work that applies FIB cutting and imaging by ions or EBSD, together with the successful computational 3D material reconstruction, we could even separate a single grain from the others. In this way we could visualize the shape of the chosen crystallite, by rotating, moving and enlarging it. Furthermore, it is possible to measure their important parameters such as grain volume, surface area, and the number of nearest neighbors. The SE images (excited by primary ion or electron beam) and the BSE images are all suitable for fast and accurate reconstruction of the grain structure, due to the channeling effect that causes differences in the intensity of differently oriented grains. If we do not restrict ourselves to the images made by ion or electron beam excited SEs or the BSEs, but we use IPF and IQ images from EBSD measurement as well, we can obtain further information about the specimen, e.g., about the highly important orientation distribution. Thus, the texture – which determines the most significant properties of a polycrystalline materials – will be recognizable in the entire explored volume, and not only in one plane. Therefore we can have complete information about the specimen. The entire explored volume ($25418.016 \mu m^3$) of the annealed nickel sheet investigated, contains 85 different grains, and 12 of them are well-reconstructable

whole uncut grains. These grains and their parameters were also presented in this chapter.

It is worth mentioning that the available minimal reconstructed volume is limited, since the minimal slice thickness is about 20 nm and the minimum of the number of slices from the smallest object is 10. Thus, materials with objects smaller than 200 nm cannot be reconstructed with such high resolution FIB tomography technique. In most of the cases the faster SE or BSE imaging for reconstruction is sufficient to obtain the necessary information. However, one should not forget that FIB tomography is a destructive material investigation technique which means that it damages the sample during the slicing process, and the explored volume of the specimen cannot be restored. Due to the time requirement of these works, as a possible future development automated serial sectioning and computer processes are recommended.

Chapter 5

Acknowledgement

First of all, I would like to thank my supervisor, Károly Havancsák for his helpful guidance. His valuable advice were very useful not only during the thesis work, but also during the past two years that I have spent in the SEM laboratory. I am grateful that I had the opportunity to learn so many new things from him.

I would like to say thanks to Gábor Varga, who taught me the usage of SEM and its the physical and operational background. Gábor helped me and gave me advice during the thesis work and my work in the laboratory.

I wish to thank Dankházi Zoltán for his clear explanations (specially regarding the operation of EBSD) all the time when I turned to him for advice. He was always helpful in both software and computational problems.

Also thanks to Szilvia Kalácska for teaching me the use of mechanical grinding and polishing apparatus and for her kind help in EBSD software evaluation methods.

I am glad that I had the opportunity to be part of this group not only from the professional viewpoint, but also in personal. I feel myself very lucky that I could work with these people.

I would like to thank to Technoorg Linda Ltd. for providing the SC-1000 SEM-Prep sample preparation equipment.

Many thanks to Enys for taking the time correcting the English of my thesis, and also for the help he gave me during my studies.

Bibliography

- [1] E. Ruska. Die elektronenmikroskopische abbildung elektronenbestrahlter oberflächen. *Z Phys.*, 83:492–497, 1933.
- [2] J. Goldstein, D.E. Newbury, D.C. Joy, Ch.E. Lyman, P. Echlin, E. Lifshin, L. Sawyer, and J.R. Michael. *Scanning Electron Microscopy and X-Ray Microanalysis*. Kluwer Academic/Plenum Publishers, third edition edition, 2003.
- [3] K. Kanaya and S. Okayama. Penetration and energy-loss theory of electrons in solid targets. *Journal of Physics D: Applied Physics*, 5(1), 1972.
- [4] S. Nishikawa and S. Kikuchi. The diffraction of cathode rays by calcite. *Proc. Imperial Acad. (Japan)*, 4:475–477, 1928.
- [5] H. Boersch. About bands in electron diffraction. (paper in german). *Physikalische Zeitschrift*, 38:1000–1004, 1937.
- [6] J.A. Venables and C.J. Harland. Electron Back Scattering patterns - new technique for obtaining crystallographic information in the scanning electron microscope. *Phil. Mag.*, 27:1193–1200, 1973.
- [7] A.J. Patkin and G.H. Morrison. Secondary ion mass spectrometric image depth profiling for three-dimensional elemental analysis. *Analytical Chemistry*, 54:2–5, 1982.
- [8] B. Tomiyasu, I. Fukuju, H. Komatsubara, M. Owari, and Y. Nihei. High spatial resolution 3D analysis of materials using gallium focused ion beam secondary ion mass spectrometry (FIB SIMS). *Nuclear Instruments and Methods in Physics Research B*, 136-138:1028–1033, 1998.

- [9] T. Sakamoto, Z. Cheng, M. Takahashi, M. Owari, and Y. Nihei. Development of an ion and electron dual focused beam apparatus for three dimensional microanalysis. *Japanese Journal of Applied Physics*, 37:2051–2056, 1998.
- [10] L. Holzer and M. Cantoni. *Review of FIB-tomography. In: I. Utke, S.S Moshkalev, Ph. Russell. Nanofabrication using focused ion and electron beams: Principles and applications.* New York: Oxford University Press., 2012.
- [11] L. Holzer, F. Indutnyi, Ph. Gasser, B. Münch, and M. Wegmann. Three-dimensional analysis of porous batio3 ceramics using fib nanotomography. *Journal of Microscopy*, 216(1):84–95, October 2004.
- [12] R.K. Bansal, A. Kubis, R. Hull, and J.M. Fitz-Gerald. High-resolution three-dimensional reconstruction: A combined scanning electron microscope and focused ion-beam approach. *Journal of Vacuum Science and Technology B*, 24:554–561, 2006.
- [13] E. de Chambost. Everhart-thornley detector. http://commons.wikimedia.org/wiki/File:Everhart-Thornley_detector.JPG, June 2007.
- [14] L.A. Giannuzzi and F.A. Stevie. *Introduction to Focused Ion Beams Instrumentation, Theory, Techniques and Practice.* Springer Science + Business Media, Inc., 2005.
- [15] L. Reimer. *Scanning Electron Microscopy - Physics of Image Formation and Microanalysis.* Springer, 1998.
- [16] A. Winkelmann. *Electron Backscatter Diffraction in Materials Science. Dynamical Simulation of Electron Backscatter Diffraction Patterns, in A.J. Schwartz, M. Kumar, B.L. Adams, D.P. Field (Editors).* Springer, 2000.
- [17] S.I. Wright, J.W. Zhao, and B.L. Adams. *Textures Microstruct.*, 13:123, 1991.
- [18] D. Juul Jensen and N.H. Schmidt. Proc. Int. Conf. Recrystallization '90, 1990.
- [19] S.I. Wright and B.L. Adams. *Metall. Trans.*, 23A:759, 1992.
- [20] J. Radon. Über die bestimmung von funktionen durch ihre integralwerte längs gewisser mannigfaltigkeiten. *Ber Verh Sächs Akad Wiss Leipzig Math-Naturw Klasse*, 69:262–267, 1917.

- [21] P.V.C. Hough. Method and means for recognizing complex patterns. <http://www.google.com/patents/US3069654>, December 18 1962. US Patent 3,069,654.
- [22] O. Engler and V. Randle. *Introduction to Texture Analysis: Macrotexture, Microtexture, and Orientation Mapping*. CRC Press, 2 edition, 2009.
- [23] EDAX-TSL. *OIM 5.3 Manual*.
- [24] Technoorg Linda Ltd. <http://www.technoorg.hu/uploads/semprep.pdf>.
- [25] G. Beilby. *Aggregation and Flow of Solids*. MacMillan & Co., London, 1921.
- [26] Zs. Radi, K. Havancsák, Sz. Kalácska, and A. Baris. Surface polishing and slope cutting by parallel ar ion beam for high-resolution EBSD measurements. Proc. of 23rd Australian Conference on Microscopy and Microanalysis and International Conference on Nanoscience and Nanotechnology 2014, 2014.
- [27] Z. Dankházi, Sz. Kalácska, A. Baris, G. Varga, Zs. Radi, and K. Havancsák. EBSD sample preparation: high energy ar ion milling. *Submitted to Materials Science Forum*.
- [28] M.D. Uchic, M.A. Groebe, D.M. Dimiduk, and J.P. Simmons. 3D microstructural characterization of nickel superalloys via serial-sectioning using a dual beam FIB-SEM. *Scripta Materialia*, 55(1):23–28, July 2006.
- [29] F.X. Lin, A. Godfrey, D. Juul Jensen, and G. Winther. 3D EBSD characterization of deformation structures in commercial purity aluminum. *Materials Characterization*, 61(11):1203–1210, November 2010.
- [30] S.J. Dillon and G.S. Rohrer. Characterization of the grain-boundary character and energy distributions of yttria using automated serial sectioning and EBSD in the FIB. *Journal of the American Ceramic Society*, 92(7):1580–1585, July 2009.
- [31] S. Morito, Y. Edamatsu, K. Ichinotani, T. Ohba, T. Hayashi, Y. Adachi, T. Furuhashi, G. Miyamoto, and N. Takayam. Quantitative analysis of three-dimensional morphology of martensite packets and blocks in iron-carbon-

manganese steels. *Journal of Alloys and Compounds*, 577(1):S587–S592,
November 2013.

[32] 3D movies. <http://adriennbaris.web.elte.hu>.